JEM Journal of Experimental Medicine

ARTICLE

Liver-X-receptor agonism enhances T cell priming and activation to promote anti-tumor immunity

Benjamin N. Ostendorf[1,3,4,5], Jonathan G. Goldstein[1,3,4], Shuang Liu[3,4], Foster C. Gonsalves[2], Jana Bilanovic[1], Mathias Yuan[1], Ji-Young Kim[1], Christopher Rouya[1], Masoud Tavazoie[2], and Sohail F. Tavazoie[1]

Many cancer patients do not benefit from current immunotherapies. This lack of efficacy may be, in part, due to insufficient priming and activation of T cells. Here, we show that activation of liver-X-receptors (LXRs) promotes adaptive anti-tumor immunity by enhancing priming of T cells. Genetic LXR deletion in the host and depletion of dendritic and CD8⁺ T cells, but not of macrophages, abrogated anti-tumor effects of LXR-agonistic therapy. In cross-presentation assays, LXR agonism promoted T cell activation upon DC/T cell cross talk. Genetic deletion of LXRs in T cells, but not in dendritic cells, blunted this effect. Dissection of the temporal dynamics of LXR-enhanced T cell effector function showed that LXR agonism rendered T cells more receptive to adopting effector states upon stimulation. Consistently, LXR agonist therapy elicited T cell expansion in cancer patients enrolled in a phase I trial. Our findings establish LXR activation as an effective approach for enhancing T cell priming.

Introduction

A major reason for the lack of immunotherapeutic efficacy in the majority of cancer patients is the absence of active T cell clones primed to eliminate cancer cells (Tumeh et al., 2014). Enhancing priming and activation of a broader repertoire of tumor-specific T cells provides a promising avenue to render immunotherapy effective in such patients (Vonderheide, 2018). Pharmacologic activation of nuclear hormone liver-X-receptors (LXRs) was recently shown to promote anti-tumor immunity by depleting immunosuppressive granulocytic myeloid-derived suppressor cells (G-MDSCs, also termed polymorphonuclear MDSC) in an *Apoe*-dependent manner (Tavazoie et al., 2018). Tumor-derived soluble factors are the main cause of expansion of MDSCs in cancer. The differential abundance of MDSC-modulating factors across different tumors contributes to a high variability in tumor-infiltrating MDSC landscapes in different patients (Gabrilovich, 2017). This heterogeneity warrants an assessment of whether LXR activation could also enhance anti-tumor immunity in patients with low MDSC infiltration.

Several groups have shown that LXR signaling can exert broad and pleiotropic effects on several immune cell types (Bensinger et al., 2008; Joseph et al., 2003; Joseph et al., 2004; Spann and Glass, 2013; Törőcsik et al., 2010). These findings motivated us to assess whether pharmacologic LXR activation could also be exploited in tumors that exhibit low recruitment of G-MDSCs. Using syngeneic breast and colon cancer models with low abundance of G-MDSCs, we herein show that pharmacologic LXR agonism promoted robust anti-tumor immunity in these models by enhancing CD8⁺ T cell priming and activation. Mechanistically, we reveal that direct LXR activation in T cells mediated this effect independent of *Apoe* expression by promoting transcriptional and chromatin accessibility states known to confer anti-tumor effector functions. Our findings reveal a second mechanism involving dendritic cell (DC)–T cell priming by which the LXR transcription factor can mediate anti-tumor immunity. LXR agonism can thus mediate anti-tumor immunity by repressing myeloid-mediated immunosuppression in an APOE-dependent manner and by enhancing DC-T cell–mediated anti-tumor immunity via an APOE-independent transcriptional mechanism.

Results

To identify an experimental system suitable for studying tumor microenvironments exhibiting low abundance of G-MDSCs, we assessed the frequency of Ly6G⁺ G-MDSCs across several syngeneic tumor models. The breast cancer E0771/E0771-DR (expressing mCherry and luciferase) and the colorectal cancer CT26 models harbored a substantially lower abundance of G-MDSCs relative to the B16F10 melanoma and the Lewis lung carcinoma

[1]Laboratory of Systems Cancer Biology, The Rockefeller University, New York, NY, USA; [2]Inspirna Inc., New York, NY, USA; [3]Department of Hematology, Oncology, and Tumor Immunology, Berlin Institute of Health, Charité-Universitätsmedizin Berlin, Berlin, Germany; [4]Berlin Institute for Medical Systems Biology (BIMSB), Max Delbrück Center for Molecular Medicine, Berlin, Germany; [5]German Cancer Consortium (DKTK), Partner Site Berlin, and German Cancer Research Center (DKFZ), Heidelberg, Germany.

Correspondence to Sohail F. Tavazoie: sohail.tavazoie@rockefeller.edu; Benjamin N. Ostendorf: benjamin.ostendorf@charite.de.

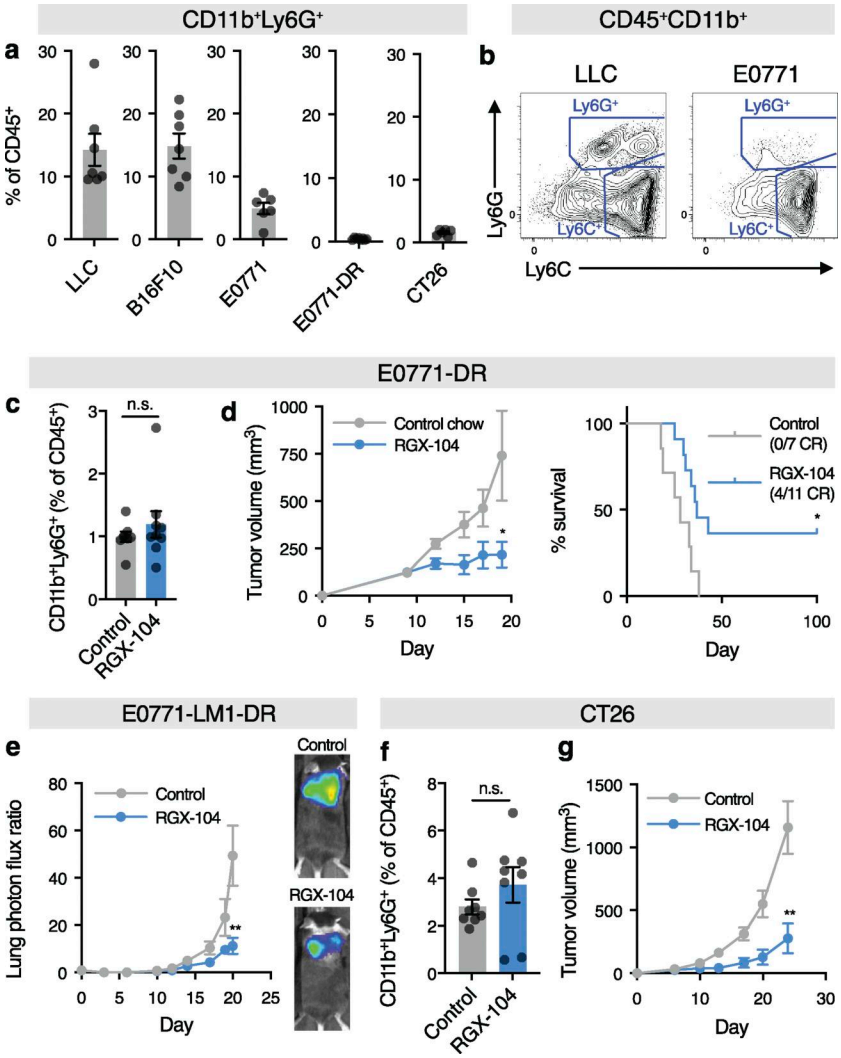

Figure 1. **LXR agonism exhibits treatment efficacy in breast and colon cancer models with low G-MDSC infiltration. (a)** Abundance of Ly6G+ G-MDSCs across different syngeneic tumor models (n = 7, 7, 6, 8, and 6 for LLC, B16F10, E0771, E0771-DR, and CT26, respectively). **(b)** Representative flow cytometry plots representing the abundance of Ly6G+ and Ly6C+ MDSCs in the LLC and E0771 tumor models. **(c)** Abundance of Ly6G+ G-MDSCs in E0771-DR tumors upon LXR-agonistic treatment with RGX-104 ($n \geq 8$ per group, two-sided t test). **(d)** Growth of orthotopic E0771-DR tumors and survival upon LXR-agonistic treatment ($n \geq 7$ per group, two-tailed t test for tumor growth and log-rank test for survival, representative of three independent experiments). **(e)** Metastatic progression of E0771-LM1-DR tumors as quantified by bioluminescence imaging (n = 7 per group, two-tailed Mann–Whitney test; images correspond to representative mice on day 20 after injection). **(f)** Abundance of G-MDSCs in CT26 tumors upon RGX-104 treatment (n = 8 per group, two-tailed t test). **(g)** Growth of CT26 tumors upon RGX-104 treatment ($n \geq 6$ per group; two-tailed t test). n.s., not significant. All experiments representative of two independent experiments unless indicated otherwise. *P < 0.05 and **P < 0.01.

(LLC) models on day 9 after tumor injection, in which we had previously observed LXR agonism to cause depletion of highly abundant G-MDSCs. (Fig. 1, a and b; and Fig. S1 a) (Tavazoie et al., 2018). Notably, although pharmacologic activation of LXRs using the synthetic LXR agonist RGX-104 did not further reduce the abundance of baseline rare G-MDSCs in the E0771-DR model as measured on day 9 after injection (Fig. 1 c), it induced complete regressions in ∼40% of mice, suggesting an MDSC-independent mechanism of action (Fig. 1 d). LXR agonism also suppressed metastatic colonization by highly metastatic E0771-LM1-DR breast cancer cells injected into the tail vein (Fig. 1 e). Similar to the E0771-DR model, RGX-104 treatment did not significantly impact the abundance of the rare Ly6G+ tumor-infiltrating MDSCs in the colorectal CT26 model (Fig. 1 f) but retained efficacy in significantly reducing tumor growth (Fig. 1 g). Myeloid Ly6C+ cells (including monocytes and monocytic MDSCs) were more abundant than G-MDSCs across all tumor models, including those with low Ly6G+ infiltration. RGX-104 treatment did not substantially modulate this subset in E0771-DR and CT26 tumors (Fig. S1, b–d). Thus, LXR agonism exerted anti-tumor efficacy in tumor models with low abundance of G-MDSCs, indicating mechanisms of action beyond depletion of these immunosuppressive cells.

We next sought to assess whether the effects of LXR agonism in tumors with low G-MDSC infiltration was mediated by the immune system. Mice that had cleared E0771-DR tumors upon LXR agonistic therapy were protected from rechallenge with unlabeled E0771 cells by both contralateral mammary fat pad injection (Fig. 2 a) and were also protected from metastatic rechallenge in tail vein metastatic colonization assays (Fig. 2 b), suggesting the generation of immunological memory upon initial LXR treatment. E0771-DR tumors from mice treated with LXR agonism exhibited increased infiltration with CD8+ T cells as assessed by immunofluorescence microscopy (Fig. 2 c). Additionally, tumor-infiltrating CD8+ T cells expressed higher levels of granzyme B in mice treated with RGX-104 in in both the E0771-DR and CT26 models as measured on day 11 after injection (Fig. 2, d–f; and Fig. S1, e–j). Consistent with adaptive immunity contributing to the anti-tumor effects of LXR agonism, efficacy of RGX-104 was largely blunted in *Rag*-deficient mice lacking adaptive immunity (Fig. 2 g) and in mice depleted of CD8+ T cells (Fig. 2 h). Thus, pharmacologic activation of LXRs induced robust anti-tumor immunity in two distinct cancer models that exhibit diminished abundance of G-MDSCs, and these effects were dependent on CD8+ T cells.

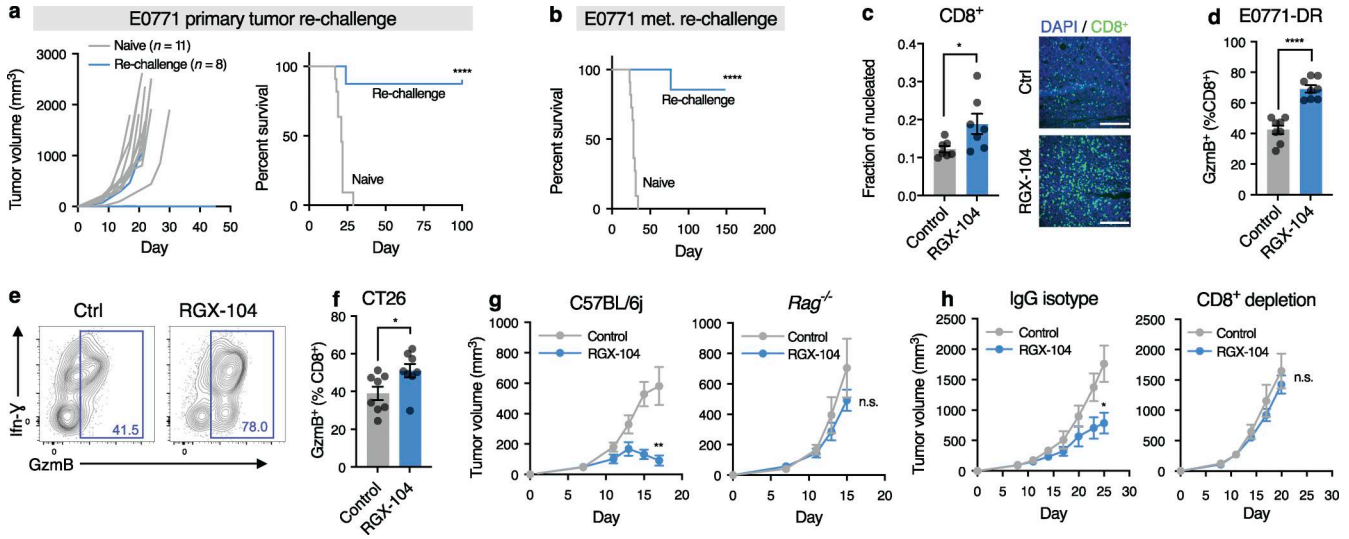

Figure 2. **LXR agonism promotes adaptive anti-tumor immunity in breast and colon cancer models. (a and b)** Tumor growth and survival of naive mice or mice that had cleared E0771-DR tumors under LXR-agonism upon contralateral primary tumor (a) or metastatic (b) rechallenge with E0771 cells ($n \geq 8$ per group, log-rank test, and data pooled from two independent experiments). **(c)** Intratumoral CD8⁺ T cell infiltration in E0771-DR tumors ($n = 7$; two-tailed t test). Images show representative sections (scale bar = 100 µm). All P values are based on two-tailed t tests. **(d–f)** Expression of granzyme B by CD8⁺ cytotoxic T cells infiltrating E0771-DR (d) and CT26 tumors (f) ($n = 8$ per group, two-tailed t test, representative of three and two independent experiments, respectively). Flow cytometry plots in e are representative for results in d. **(g)** Growth of E0771-DR mammary fat pad tumors in C57BL/6J wild-type versus Rag$^{-/-}$ mice ($n \geq 4$ per group; two-tailed t test; representative of two independent experiments). **(h)** Growth of E0771-DR mammary fat pad tumors upon depletion of CD8⁺ cells ($n \geq 6$ per group, two-tailed t test; representative of two independent experiments). *P < 0.05 and ****P < 0.0001.

We next investigated the stage of the immune response at which LXR signaling stimulates adaptive immunity in tumor models lacking substantial G-MDSC infiltration. To this end, we assessed whether RGX-104 elicited immune activation in the tumor-draining LN (DLN) upstream of T cell effector activity or tumor cell killing in the tumor microenvironment (Chen and Mellman, 2013). Interestingly, as assessed on day 9 after tumor cell injection in mice treated with the LXR agonist, CD4⁺ and CD8⁺ T cell compartments shifted from a naïve to a CD62L^{lo}CD44^{lo} phenotype in both the E0771-cOC and CT26 models, likely representing recently described pre-effector T cells critically required for efficient anti-tumor immunity (Nakajima et al., 2021) (Fig. 3, a–c; and Fig. S2, a and b). Such pre-effector CD62L^{lo}CD44^{lo} T cells have been shown to be activated but have not yet upregulated the effector/memory program (Nakajima et al., 2021).

To more comprehensively profile T cells in the tumor DLNs, we isolated T cells using flow cytometry and performed combined single-cell RNA-sequencing (scRNAseq) and TCR-sequencing (TCRseq) on day 8 after injection. To this end, we pooled T cells and APCs isolated by flow cytometric sorting from eight control mice and from eight mice treated with RGX-104 (Fig. S2, g–n). By leveraging TCRseq we were also able to determine T cell clonality in dLN-resident T cells. RGX-104–treated mice showed increased clonal expansion of effector T cells expressing cytotoxic marker genes (Fig. 3, d–f), consistent with LXR activation enhancing the adoption of effector states by T cells. These dLN-resident effector T cells likely represent the source of the increased population of tumor-resident effector T cells characterized by expression of granzyme B (Fig. 2 f).

APCs, in particular DCs, are critically required for the priming of cytotoxic T cells in tumor-DLNs (Roberts et al., 2016). We therefore also assessed whether RGX-104 treatment enhanced activation of specific APC subsets, including macrophages and several DC subsets. In mice receiving LXR agonistic treatment, all major APC subsets in the DLN showed higher expression of MHC class II, including macrophages, and three DC subsets (CD11b⁺, CD8⁺, and CD103⁺ DCs) in the E0771-cOC and CT26 models on day 9 after injection, indicating increased activation (Fig. 3, g–i; and Fig. S2, c–e). Additionally, both macrophages and CD103⁺ DCs showed upregulation of the costimulatory molecules CD40 and CD86 under LXR agonism. The use of mCherry-expressing E0771-cOC cells allowed us to also assess the uptake of tumor-derived antigen by APCs (Fig. S2 f) (Broz et al., 2014). DLN-resident APCs in RGX-104–treated mice displayed enhanced ingestion of tumor-derived antigen, as indicated by increased mCherry-signal (Fig. 3 g). The impact of LXR agonism on tumor resident as opposed to DLN-resident APCs was not uniform across different APC subsets and tumor models, although we noticed increased expression of some activation markers on specific APC subsets in each model (Fig. S3, a–c). To assess the impact of LXR activation on DLN-resident APCs regarding recently identified tolerogenic signatures elicited by LXR agonism in cDC1 subsets (Bosteels et al., 2023), we isolated them by flow cytometry on day 8 after tumor injection and performed single-cell transcriptional profiling. We observed moderate suppression, rather than upregulation, of some genes making up the tolerogenic signature (Fig. S3, d–g). Assessment of the recently described mReg signature did not show major changes upon LXR agonism (Fig. S3, h and i) (Maier et al., 2020). This signature was not specific to any cell cluster. In sum, LXR agonistic therapy enhanced activation of several APC subsets and enhanced priming of T cells in tumor DLNs.

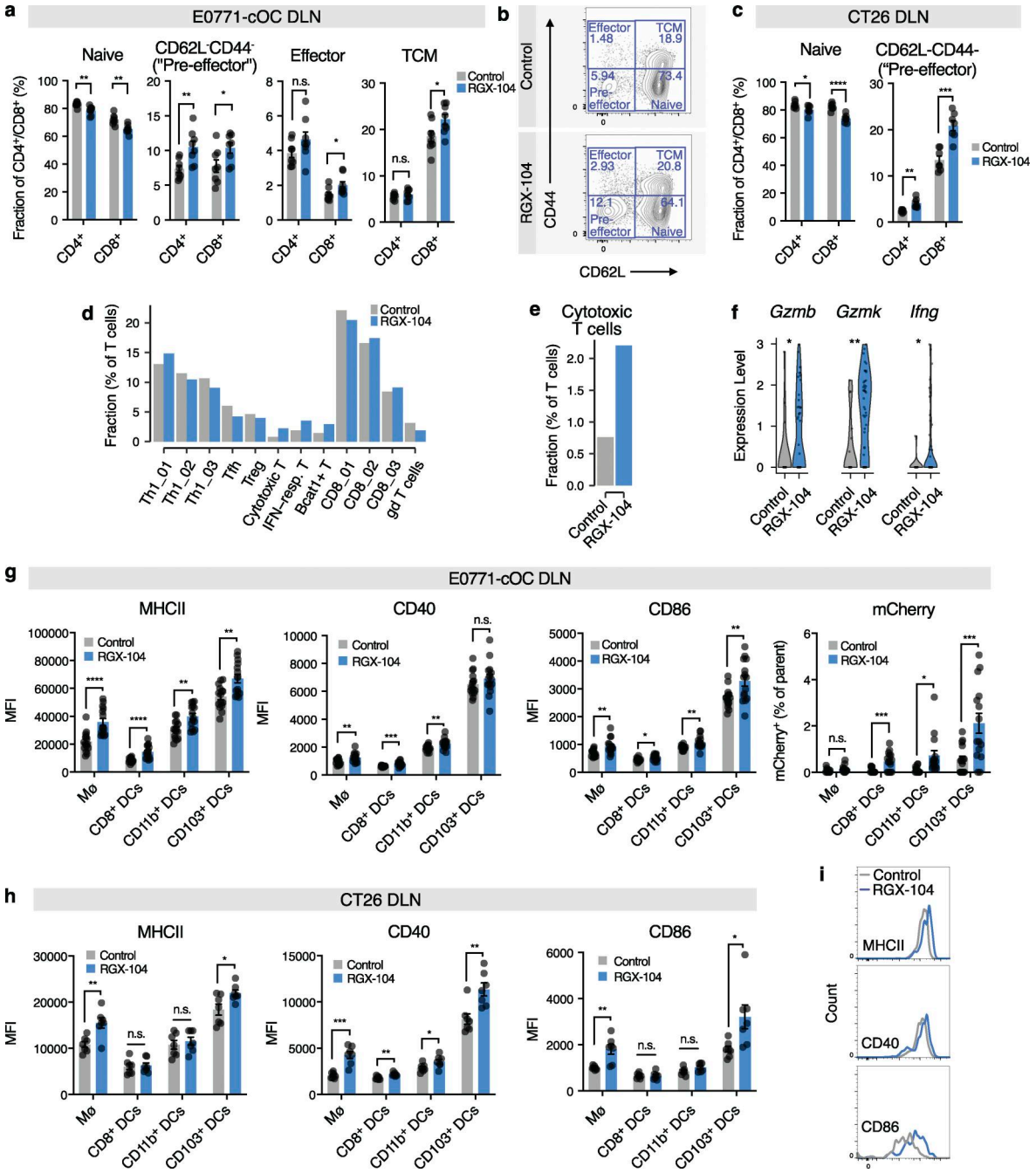

Figure 3. **LXR agonism enhances immune activation in tumor DLNs. (a–c)** Phenotype of DLN-resident CD4⁺ and CD8⁺ T cells in E0771-cOC (a) or CT26-DR (c) tumor-bearing mice treated with RGX-104 (n = 8 and 7 per group, respectively, two-tailed t tests; representative of two independent experiments). Flow cytometry plots in b show representative samples gated for CD8⁺ T cells from a. **(d–f)** Proportion of all T cell subsets (d) and only cytotoxic T cells (e) out of all T cells in E0771-DR tumor DLNs as assessed by scRNAseq. **(f)** Comparison of the expression of select canonical effector genes in cytotoxic T cells in control versus RGX-104–treated mice (P values according to Mann–Whitney tests). **(g–i)** Activation status of APCs in the LNs draining E0771-cOC (g) and CT26 (h) tumors (n = 15 [g] and 7 [h] per group; two-tailed t tests, each representative of two independent experiments). **(i)** Representative plots from h showing expression of MHCII, CD40, and CD86 in CD103⁺ DCs. MHCII, MHC class II. *P < 0.05, **P < 0.01, ***P < 0.001, and ****P < 0.0001.

We next sought to assess whether DCs or macrophages were critical for LXR agonistic anti-tumor activity. To this end, we used mice transplanted with bone marrow expressing diphtheria toxin (DT) receptor (DTR) under the control of the *Itgax* promoter, which allowed for the selective depletion of CD11c⁺ APCs (Fig. 4 a) (Jung et al., 2002). RGX-104 did not show any therapeutic activity in CD11c-depleted mice (Fig. 4 b), underscoring CD11c⁺ APCs to be essential for the promotion of anti-tumor activity elicited by LXR agonism. In the tumor microenvironment, macrophages frequently co-express CD11c (Broz et al., 2014), and consistent with this previous finding, we observed depletion of intratumoral, but not of DLN-resident, macrophages in *Itgax*^{DTR}

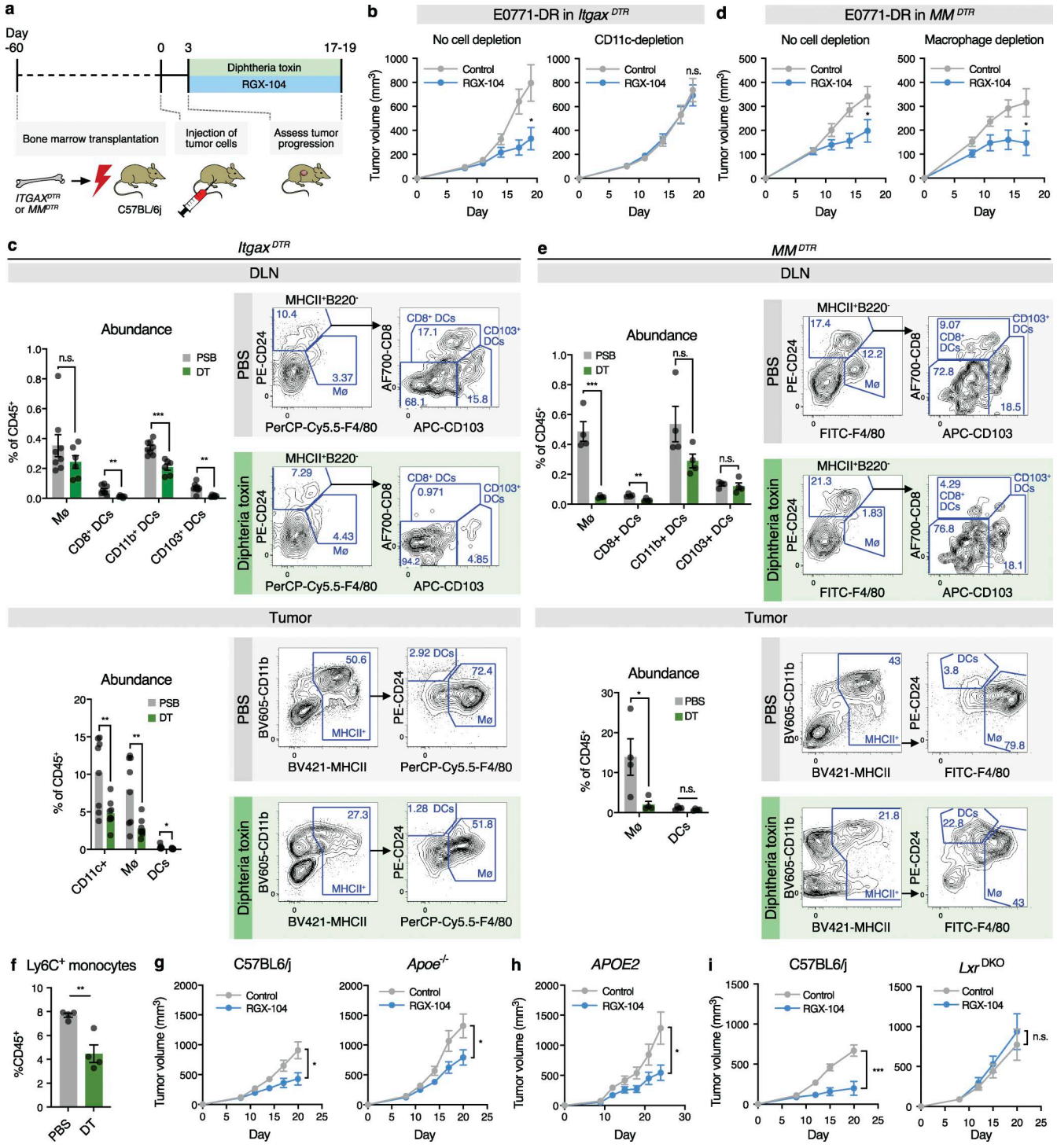

Figure 4. **LXR agonistic therapy critically depends on CD11c⁺ DCs and host *Lxr* but not *Apoe* expression. (a)** Schematic of strategy for in vivo depletion of APC subsets. **(b)** Growth of orthotopic E0771-DR tumors in the presence or absence of CD11c⁺ cells as outlined in a (n = 14–16 per group, two-tailed t test, data pooled from two independent experiments). **(c)** Abundance of APC subsets in tumor DLNs and tumors of E0771-DR tumor bearing–mice transplanted with *Itgax*-DTR bone marrow and treated with PBS or DT (two-tailed t tests). Images show representative flow cytometry plots (n = 6–8 per group, two-tailed t tests). **(d)** Growth of orthotopic E0771-DR tumors in the presence or absence of LyzM⁺Csf1r⁺ cells (n = 7–9 per group, two tailed t test, representative of two independent experiments). **(e)** Abundance of APC subsets in DLNs or tumors of E0771-DR tumor bearing–mice transplanted with MM-DTR bone marrow and treated with PBS or DT (two-tailed t tests). Images show representative flow cytometry plots (n = 4 per group, two-tailed t tests). **(f)** Fraction of Ly6C⁺ monocytes out of CD45⁺ cells in peripheral blood of MM-DTR mice treated with either PBS or DT (n = 4 per group, P value according to one-sided T test). **(g)** Growth of E0771-DR in C57BL/6J wild-type versus *Apoe*-KO mice ($n \geq 11$ mice per group, respectively; data pooled from two independent experiments). **(h)** Growth of E0771-DR tumors in *APOE2*-knock-in mice ($n = \geq 15$ mice per group; two-tailed t test). **(i)** Growth of E0771-DR tumors in C57BL6/J wild-type versus *Lxr*-DKO mice ($n \geq 10$ mice per group, representative of two independent experiments; two-tailed t test). MHCII, MHC class II. *P < 0.05, **P < 0.01, and ***P < 0.001.

transplanted mice upon DT administration (Fig. 4 c). Therefore, to differentiate whether macrophages contributed to the anti-tumor effect of RGX-104, we employed the *LyzM*^{Cre} × *Csf1r*$^{LSL\text{-}DTR}$ model (hereafter referred to as *MM*^{DTR}), which allows for the specific depletion of monocytes and macrophages (Schreiber et al., 2013). Despite efficient depletion of macrophages in both the tumor and DLN in this model, RGX-104 retained its anti-tumor activity (Fig. 4, d and e). Notably, we also observed significant depletion of monocytes as observed by others (Schreiber et al., 2013) (Fig. 4 f). Thus, LXR agonistic therapeutic efficacy critically relied on CD11c$^+$ DCs, but not on macrophages or monocytes.

We next sought to define the molecular underpinnings of LXR-mediated enhancement of anti-tumor immunity. In models of melanoma and lung cancer, LXR agonistic therapy was previously shown to promote anti-tumor immunity by depleting G-MDSCs in an Apoe-dependent manner (Tavazoie et al., 2018). Consistent with an Apoe-MDSC axis-independent effect occurring, in the E0771-DR model, LXR agonism exhibited anti-tumor activity in *Apoe*$^{-/-}$ mice (Fig. 4 g). Additionally, RGX-104 also exerted anti-tumor activity in mice expressing the hypomorphic human *APOE2* variant, in which we previously observed complete abrogation of LXR agonist efficacy in melanoma models, which contain high G-MDSC infiltration (Fig. 4 h) (Ostendorf et al., 2020). Consistent with LXR activation eliciting anti-tumor immunity independent of Apoe in the tumor models described here, DLN-resident CD11c$^+$-enriched cells from *Apoe*$^{-/-}$ mice showed enhanced, rather than suppressed, expression of activation markers and genes implicated in antigen processing (Fig. S4, a and b), and RGX-104 enhanced conversion of T cells into an effector state in *Apoe*-deficient mice (Fig. S4 c). Because Apoe was previously shown to enhance DC priming of NKT cells via the Ldlr receptor (Elzen et al., 2005), we also assessed response to RGX-104 in mice lacking CD1d$^+$ NKT cells and in mice transplanted with *Ldlr*-deficient bone marrow. LXR agonism exerted therapeutic activity in both contexts, ruling out a role for CD1d$^+$ NKT cells in this response (Fig. S4, d and e). Together, these results are consistent with LXR agonistic therapy enhancing T cell priming and anti-tumor activity through mechanisms beyond the Apoe/MDSC axis in the models exhibiting low G-MDSC infiltration studied here.

To assess whether RGX-104 activity depends on tumoral or non-tumoral LXRs, we next compared treatment responses in wild-type versus *LXR*-double KO (*LXR*^{DKO}) mice, lacking both Lxrα and Lxrβ receptors. Treatment efficacy was completely abrogated in *LXR*^{DKO} mice injected with LXR-competent tumors, indicating that RGX-104 acted specifically via its impact on LXRs expressed by non-tumoral host cells rather than on tumor LXRs (Fig. 4 i).

To determine the mechanism through which activation of LXRs enhanced T cell activation, we assessed DC and T cell responses to RGX-104 in vitro. Treatment of bone marrow–derived DCs (BMDCs) with RGX-104 in isolation did not enhance the expression of activation markers (Fig. S5 a), indicating that enhanced activation of APCs upon RGX-104 treatment in vivo may require additional cellular or microenvironmental components. We, therefore, next assessed the impact of RGX-104 on OT-I CD8$^+$ T cells co-cultured with BMDCs that had been pulsed with an OVA-derived peptide. Transcriptional profiling of flow cytometry–sorted OT-I T cells after co-culture with BMDCs revealed that multiple T cell activation–related pathways became upregulated in RGX-104–treated T cells (Fig. 5, a and b; and Fig. S5, b and c). As part of this activation pattern, several genes implicated in T cell effector function, including *Ifng* and *Gzmb*, were upregulated (Fig. 5 c). We validated this finding by assessing IFN-γ and granzyme B induction at the protein level by flow cytometry after 24 h of co-culture (Fig. 5 d). These findings as a whole reveal that RGX-104 enhances T cell activation in the context of cross-priming by BMDCs.

We next assessed in which cell compartment LXR activation mediated enhanced T cell activation. To specifically study the effect of genetic deletion of LXRs in DCs versus in T cells, we generated BMDCs from *LXR*^{DKO} mice and crossed *LXR*^{DKO} mice with OT-I mice to generate *LXR*^{DKO} OT-I T cells. Strikingly, KO of LXRα and LXRβ in T cells, but not in BMDCs, blunted RGX-104–mediated promotion of T cell activation in cross-priming assays (Fig. 6 a). These results indicate that activation of LXR signaling in CD8$^+$ T cells, rather than in DCs, enhanced T cell activation. To further characterize the molecular mechanism downstream of LXR activation in T cells, we performed transcriptomic and chromatin accessibility profiling in T cells activated in a co-culture with *LXR*^{DKO} DCs after 19 h of co-culture. Transcriptional and chromatin profiling revealed a significant overlap of genes, as exemplified by *Ifng*, encoding IFN-γ (Fig. 6 b and Fig. S5 d). Importantly, pathway analysis in this assay with *LXR*^{DKO} DCs revealed T cell activation as the top enriched pathway (Fig. S5 e), similar to our results from using LXR-proficient DCs (Fig. 5 b and Fig. S5 f), again supporting LXR activation in T cells rather than in DCs as mediating these effects. Analysis of genes implicated in T cell co-stimulation, co-inhibition, and effector functions revealed enhanced expression and increased chromatin accessibility for several genes with roles in T cell co-stimulation and effector function (Fig. 6 c). Analysis of motif enrichment in differentially accessible chromatin promoter regions revealed enrichment of AP-1 and Nfkb transcription factor–binding sites, which have previously comprehensively been implicated in T cell activation and which may serve as potential downstream mediators of RGX-104 effects (Fig. S5 g) (Yukawa et al., 2019; Thaker et al., 2015). In sum, these data demonstrate that RGX-104–mediated activation of LXRs in T cells promotes an effector phenotype with comprehensive remodeling of the T cell chromatin landscape. Since these data cannot decouple primary from secondary indirect effects of LXR activation, we also performed CUT&Tag profiling (Kaya-Okur et al., 2019), which identified binding of LXRβ to the promoter region of several genes previously shown to enhance T cell effector functions, including *Nfatc2* (Peng et al., 2001), *Jaml* (McGraw et al., 2021), *Cd226* (Weulersse et al., 2020), and *Crtam* (Yeh et al., 2008) (Fig. S5, h and i). Thus, these genes represent candidate genes that may link LXR signaling to enhancement of T cell effector states.

We next sought to dissect the stage at which LXR agonism promotes T cell activation. To this end, we treated naïve CD8$^+$ T cells in isolation at different time points relative to CD3/CD28 ligation and RGX-104 treatment (Fig. 6 d). LXR activation

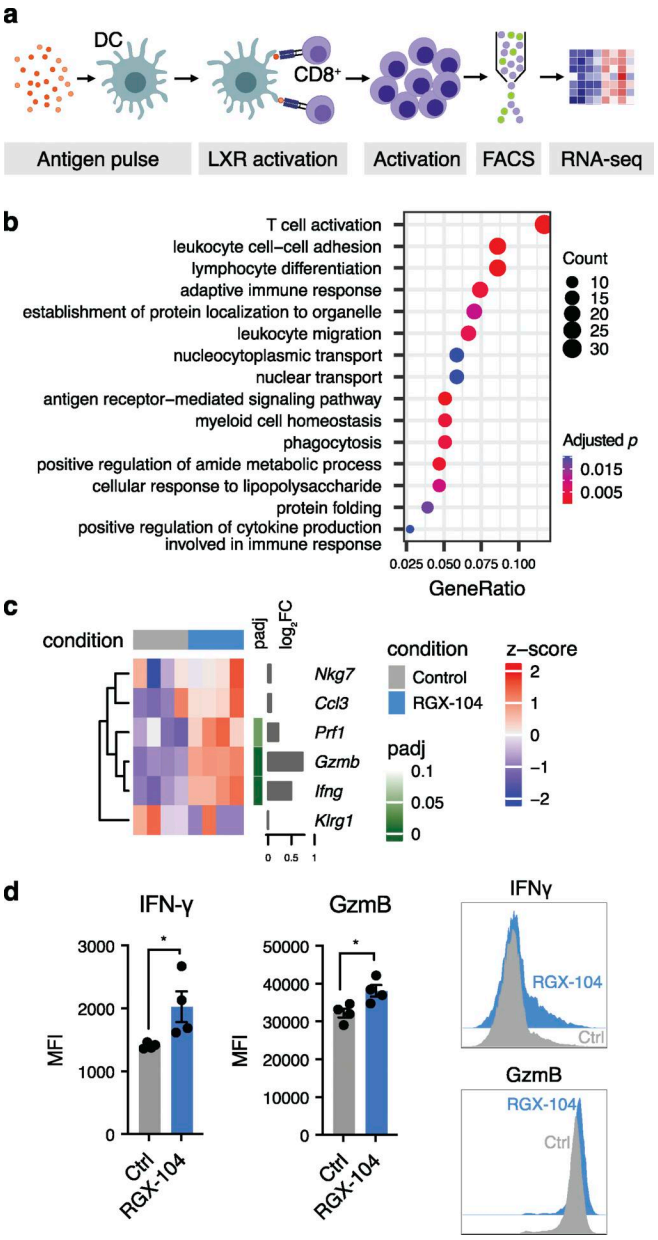

Figure 5. **LXR agonism promotes T cell activation. (a)** Schematic of experimental approach to assess the impact of pharmacologic LXR activation on T cell priming and activation in vitro. **(b)** Gene ontology pathway enrichment analysis in genes significantly upregulated in RGX-104–treated OT-I T cells. **(c)** Expression of genes implicated in T cell effector function in RGX-104–treated OT-I T cells as assessed by RNAseq (n = 4 per group; Wald test, adjusted by false discovery rate). **(d)** Expression of IFN-γ and granzyme B in OT-I CD8$^+$ T cells after co-culture with antigen-pulsed BMDCs as assessed by flow cytometry (n = 4 per group, representative of three independent experiments, two-tailed t tests). Plots on the right show representative samples. *P < 0.05.

increased the fraction of CD44$^-$CD62L$^-$ "pre-effector" and CD44$^+$CD62L$^-$ effector cells in non-stimulated cells and in cells that were treated with RGX-104 simultaneous with CD3/CD28 stimulation, mirroring our in vivo findings (Fig. 6, e and f; and Fig. S5 j). Pre-treating T cells with RGX-104 only prior to CD3/CD28 stimulation also induced robust conversion of T cells into pre- and effector states with enhanced expression of granzyme B and IFN-γ, while treating cells only upon initiating CD3/CD28 stimulation after the same initial resting phase before CD3/CD28 stimulation did not show this effect. These findings indicate that LXR activation in CD8$^+$ T cells conditions them to be more receptive to adopting effector states upon subsequent stimulation.

To characterize this conditioned state more comprehensively, we subjected naïve T cells treated with RGX-104 versus control to transcriptional and chromatin accessibility profiling. As expected, expression and chromatin accessibility increased of genes implicated in cholesterol and lipid metabolism (Fig. 7, a–d). Interestingly, chromatin accessibility for *Sell* (encoding L-selectin/CD62L) and *GzmB* (encoding granzyme B) significantly decreased and increased, respectively, in RGX-104–treated cells, while expression as assessed by RNAseq did not differ significantly (Fig. 7 e). These data suggest that the LXR-induced pre-effector state may primarily be reflected at the chromatin or "epigenetic" rather than transcriptional level.

We next assessed whether combining LXR agonism with other treatment modalities could provide additional therapeutic benefit. While the combination of RGX-104 with a CD40-activating antibody yielded minimal cooperativity (Fig. 8, a and b), combining radiotherapy with LXR agonism showed a pronounced additive effect (Fig. 8 c).

Lastly, we assessed data from a currently ongoing phase 1b study (NCT02922764) investigating the use of RGX-104 as monotherapy or in combination with docetaxel or immune checkpoint inhibition (either anti-CTLA4 or anti-PD1) in patients with metastatic cancer (Fig. 9 a). Consistent with RGX-104 leading to T cell activation in humans, patients receiving RGX-104 therapy exhibited expansion of multiple T cell clones in the peripheral blood (Fig. 9 b). RGX-104–treated patients also exhibited multiple newly detected T cell clones, consistent with RGX-104 therapy promoting T cell priming (Fig. 9 c). The number of expanded T cell clones as well as the number of newly detected T cell clones did not differ significantly depending on whether patients also received immune checkpoint blockade. Notably, the number of rearranged TCR regions increased significantly on-treatment relative to pre-treatment (Fig. 9 d). Thus, RGX-104 treatment associated with T cell expansion and increased clonal richness in humans, consistent with our findings in preclinical mouse models.

Discussion

Currently approved immune checkpoint therapies are highly effective in some but not the majority of patients. Therefore, orthogonal clinical approaches to eliciting anti-tumor immunity are needed.

Here, we show that LXR agonistic treatment activates T cell–mediated immunity in preclinical models exhibiting low abundance of G-MDSCs, depletion of which was a major mechanism driving anti-tumoral effects of LXR agonism in models with high G-MDSC infiltration (Tavazoie et al., 2018). We employed a combination of genetic and pharmacologic in vivo and in vitro approaches to identify LXR agonism to directly enhance activation and effector differentiation of T cells upon stimulation to mediate anti-tumor immunity in these models.

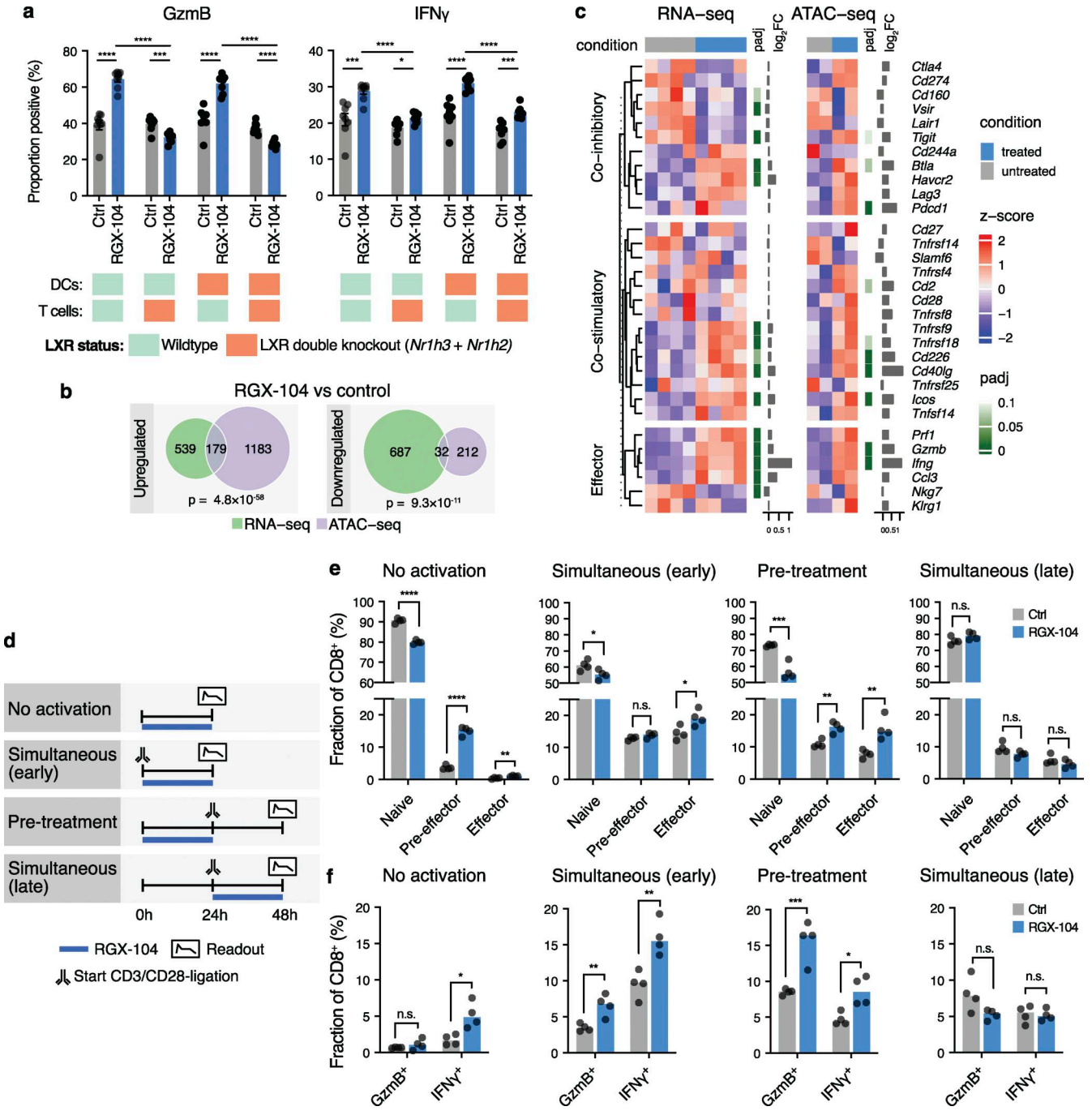

Figure 6. **LXR agonism renders CD8⁺ T cells more receptive to adopting effector functions through LXR activation in CD8⁺ T cells. (a)** Expression of IFN-γ and granzyme B in OT-I CD8⁺ T cells after co-culture with antigen-pulsed BMDCs as assessed by flow cytometry (n = 8 per group, representative of two independent experiments, two-tailed t tests). **(b)** Overview of differential gene expression and accessible chromatin regions in RGX-104–treated OT-I CD8⁺ T cells co-cultured with LXR^{DKO} BMDCs upon RGX-104 treatment as assessed by RNAseq and ATAC-seq (hypergeometric tests). **(c)** Expression and chromatin accessibility of genes implicated in T cell effector function, co-inhibition, and co-stimulation in RGX-104– versus control-treated OT-I T cells from b. **(d)** Schematic of in vitro treatment of primary naive CD8⁺ T cells in relation to activation by CD3/CD28 ligation. **(e)** Fractions of naive (CD44⁻CD62L⁺), pre-effector (CD44⁺CD62L⁻), and effector (CD44⁺CD62L⁻) CD8⁺ T cells as determined by flow cytometry. **(f)** Expression of effector molecules in CD8⁺ T cells as determined by flow cytometry. *P < 0.05, **P < 0.01, ***P < 0.001, and ****P < 0.0001.

LXRs are transcription factors with historically defined roles in the regulation of cholesterol and lipid metabolism upon sensing of oxysterols. LXRs have been implicated in various immunological processes, including autoimmunity, antibacterial defense, and anti-tumoral immunity (Tavazoie et al., 2018; Joseph et al., 2004; Korf et al., 2009; Ito et al., 2016; Westerterp et al., 2017). Given their diverse actions on different cell types, we postulated that LXRs might exert anti-tumor immunological effects also in hosts with scarce MDSC infiltration. The identification of two independent models with particularly low

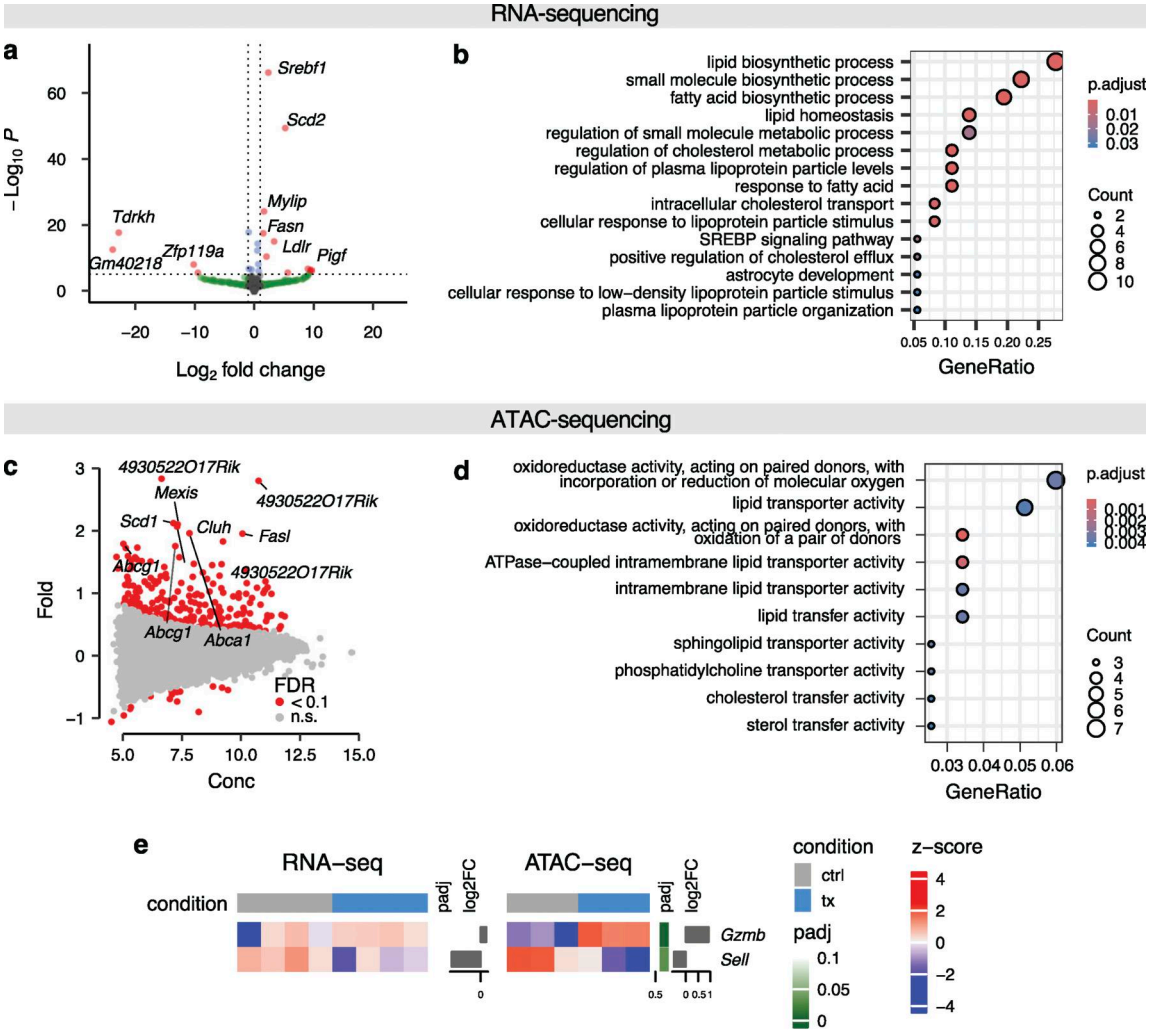

Figure 7. **Transcriptional and chromatin accessibility profiling of naive CD8⁺ T cells upon LXR activation. (a)** Volcano plot showing differentially expressed genes in naive CD8⁺ T cells treated with the LXR agonist RGX-104 for 24 h as assessed by RNAseq (n = 4 per group). **(b)** Gene ontology pathway analysis of significantly upregulated genes from a. **(c)** MA-plot of differential chromatin accessibility in naive CD8⁺ T cells treated with the LXR agonist RGX-104 for 24 h (n = 3 per group). **(d)** Gene ontology pathway analysis of genes in proximity to differentially accessible chromatin regions from c. **(e)** Heatmap showing gene expression and chromatin accessibility changes for *Gzmb* and *Sell* in CD8⁺ T cells from a–d.

G-MDSC infiltration allowed us to uncover an additional anti-tumoral mechanism of LXR agonism based on promoting the adoption of effector states in CD8⁺ T cells. Thus, our data extend the potential use of therapeutic LXR agonism to cancer patients with low degrees of MDSC-mediated immune suppression but who lack efficient T cell activity. What is the mechanistic basis of anti-tumoral activity underlying MDSC-independent anti-tumor immunity? Several groups have shown that LXR activation in tumors can promote anti-tumoral effects (Fukuchi et al., 2004; Candelaria et al., 2014; Guo et al., 2011; Guilbaud et al., 2023). In our study, genetic deletion of LXRα and LXRβ in the host completely abrogated treatment efficacy, indicating that the impact of LXR activation in tumor cells is negligible for treatment efficacy in the models studied herein, with the effect likely being more prominent in other models. Macrophages have been shown to mediate immunological effects of LXR signaling in different contexts and thus also represented potential mediators of the effects observed in this study (Joseph et al., 2004; Carbo et al., 2021; Sohrabi et al., 2020). In addition, many studies have shown that cholesterol efflux pathways modulate the phenotype of tumor-associated macrophages, providing another potential mechanistic explanation for our findings (Zamanian-Daryoush et al., 2013; Goossens et al., 2019). However, genetic mouse models that enabled the specific depletion of macrophages versus all CD11c⁺ cells allowed us to demonstrate that macrophages are unlikely to be major mediators of LXR agonistic treatment efficacy in the models studied here.

Using in vitro cross-presentation assays, we found that LXR agonism promotes CD8⁺ T cells effector states. Employing genetic deletions and assessing T cell states upon LXR treatment in isolation, we observed that LXR agonism directly acts on CD8⁺ cells to render them more receptive to adopting effector states. Importantly, several studies have previously assessed the impact of LXR signaling on different facets of T cell biology. Regarding proliferation, T cells exhibited a proliferative advantage in whole-body LXRβ-deficient mice, which was shown to be mediated by

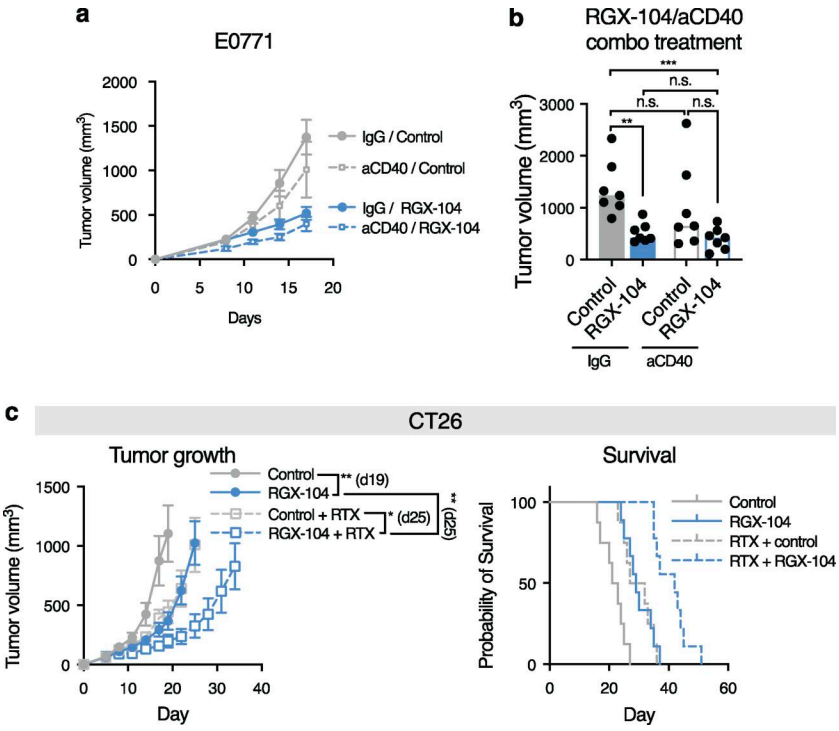

Figure 8. **LXR agonism and radiotherapy act additively. (a)** Tumor growth of mice injected with E0771 tumor cells and treated with RGX-104 and either IgG control or anti-CD40 antibody (n = 7 per group). **(b)** Tumor volumes of mice from a on day 17 after injection. **(c)** Tumor growth and survival of mice injected with CT26 tumor cells and treated with RGX-104 and radiotherapy (n = 8 per group, two-tailed t test; representative of two independent experiments). *P < 0.05, **P < 0.01, and ***P < 0.001.

Abcg1 (Bensinger et al., 2008; Armstrong et al., 2010). In contrast with this, recent work utilizing mixed bone marrow chimeras showed that LXRβ deficiency specifically in T cells reduced T cell proliferation (Michaels et al., 2020). A different study showed T cell–specific deletion of LXRs did not alter T cell proliferation (Chan et al., 2020). Our findings regarding enhanced effector states upon LXR agonism are consistent with a recent study that found LXRβ to be required for fitness of effector T cells (Michaels et al., 2020). However, our in vitro studies show that pharmacological LXR activation enhances effector states beyond fitness increases. Overall, differences in the specific phenotypes found to be affected by LXR signaling across different studies may be due to the mode of T cell activation and the difference between genetic LXRβ deletion versus pharmacologic LXR activation. It is interesting to note that our in vivo experiments revealed an increase in both T cells with a pre-effector $CD44^{(lo)}CD62L^{-}$ phenotype and an

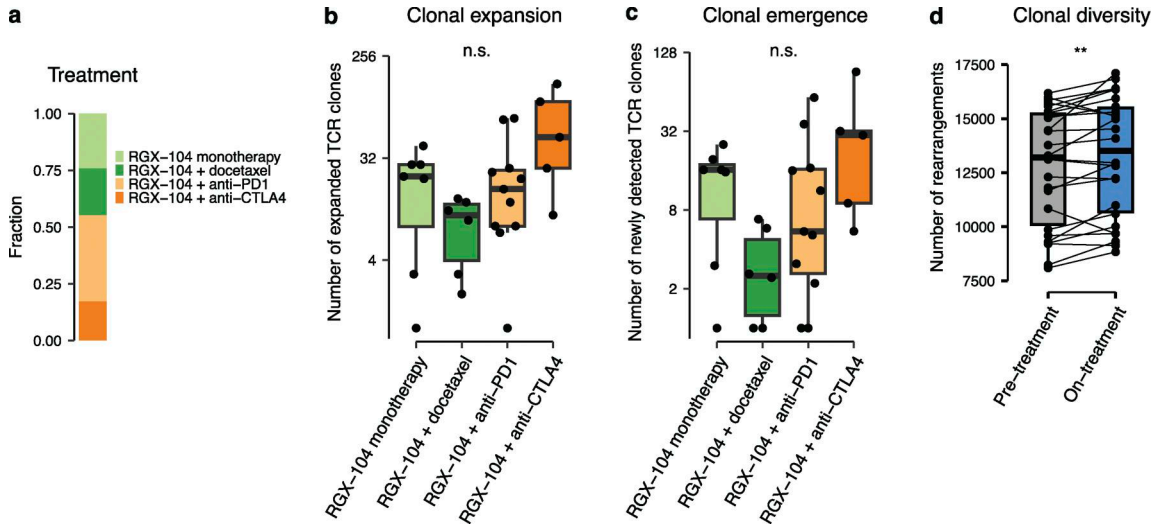

Figure 9. **RGX-104 treatment is associated with clonal T cell expansion and enhanced TCR diversity in relapsed/refractory cancer patients. (a)** Fraction of patients receiving given therapies. **(b)** Number of expanded TCR clones in the peripheral blood of patients after one cycle (28 days) of treatment as indicated. **(c)** Number of newly detected TCR clones in peripheral blood after one cycle of treatment as indicated. **(d)** Longitudinal analysis of richness of TCR repertoire as measured by $\log_2$ of productive rearrangements of peripheral clones following treatment with RGX-104 relative to pre-treatment. Boxplot whiskers in b and c extend to the smallest and largest value within 1.5 times the interquartile ranges of the hinges, and box center and hinges indicate median and first and third quartiles, respectively. For logarithmic display of data in b and c, a count of 1 was added to all data points. **P < 0.01.

increase in cytotoxic effector T cells. Our in vitro time course experiments suggest that LXR agonism facilitates the adoption of a pre-effector state, which renders T cells more receptive to priming and differentiating into cytotoxic effector cells.

Intriguingly, several other studies have previously implicated cholesterol metabolism in shaping T cell function. Cholesterol accumulation in T cells is associated with exhaustion phenotypes and blunted activation. Consistently, reducing cholesterol biosynthesis enhanced T cell function (Ma et al., 2019). In a separate study and consistent with other reports, lowering cellular cholesterol levels via *Fibp* genetic deletion promoted T cell anti-tumor function (Zhang et al., 2022). Prior to these findings, two studies showed that cholesterol and cholesterol sulfate can inhibit TCR signaling (Swamy et al., 2016; Wang et al., 2016), and lowering cholesterol levels in T cells promoted expression of IFN gene signatures (Yan et al., 2023). These data are consistent with our work, in which LXR agonistic therapy, which promotes cholesterol efflux, led to enhanced T cell activation. In contrast, one study found that inhibition of cholesterol esterification enhanced anti-tumor cell responses (Yang et al., 2016). In addition, the recent study that found cholesterol deficiency in T cells may activate IFN signaling also reported inhibited proliferation and increased apoptosis in T cells upon LXR activation (Yan et al., 2023). Our data from in vivo and T cell/DC cross-priming assays show the net effect of LXR activation to result in enhancement of T cell activation. Notably, the impact of altering cellular cholesterol levels seem cell type specific, as shown for differential effects of perturbing cholesterol levels in $CD4^+$ T helper cells and γδ-T cells as compared with $CD8^+$ T cells (Surls et al., 2012; Cheng et al., 2013). Overall, these data indicate that the role of cholesterol, analogous to LXRs, is context- and cell type–dependent and that effects may depend on the specific perturbation of cholesterol metabolism. It remains to be seen whether the enhancement of $CD8^+$ effector states that we observed herein are mediated by altered cholesterol levels or via direct LXR signaling effects.

One previous study indicated that LXR agonists released by tumor cells could dampen migration of DCs to tdLNs, which is at odds with our findings of enhanced APC activation and undiminished DC migration in vivo upon pharmacological LXR activation (Villablanca et al., 2009). Importantly, the authors of this previous study focused on tumor-derived LXRα agonists, which may explain the differences with our findings, which are based on pharmacological and predominantly LXRβ-targeted activation. Our in vitro studies suggest that more active APC states upon in vivo LXR activation may be secondary to promotion of the tumor immunity cycle by enhancing T cell activation rather than mediated by a direct effect of LXR agonism on APC function. However, other studies found LXR signaling to enhance DC trafficking, and we cannot rule out that promotion of DC function contributes to enhancing anti-tumor immunity upon pharmacological LXR activation (Beceiro et al., 2018).

Limitations

While our study demonstrates a direct action of LXR activation on T cell state, future work is needed to characterize the elicited conditioned pre-effector state further and to identify the molecular mechanisms mediating this impact. It will also be important to assess how LXR activation impacts T cell exhaustion and dysfunction in the tumor microenvironment. In addition, while our in vitro experiments demonstrate that LXR agonism acts directly on T cells to render them more receptive to priming, we cannot rule out that additional effects contribute to enhanced anti-tumor immunity upon LXR activation. Our findings from a phase I trial suggest that promotion of T cell anti-tumor immunity upon LXR activation is likely also taking place in humans. One limitation of these data is that we could not assess the impact of LXR agonistic therapy on $CCR7^+$ DCs and G-MDSCs.

In sum, our work identifies LXR agonism as a means of enhancing T cell immunity via a mechanistically orthogonal and complementary therapeutic approach to established immunotherapies, providing a potential path for augmenting existing immunotherapeutic approaches in cancer.

Materials and methods

Animal studies

All studies involving animals were performed in accordance with a protocol approved by the Institutional Animal Care and Use Committee at The Rockefeller University and at Charité University Medicine Berlin. C57BL/6J (strain no. 000664), *Rag1*-KO (no. 002216), $Itgax^{DTR/EGFP}$ (no. 004509), $Csf1r^{DTR/mCherry}$ (no. 024046), $Lyzm^{Cre}$ (no. 004781), *Apoe*-KO (no. 002052), *Cd1d*-KO (no. 008881), *Ldlr*-KO (no. 002207), and OT-I (no. 003831) mice were obtained from The Jackson Laboratory. Human *APOE2* knock-in mice were from Taconic (no. 1547). $Csf1r^{DTR}$/*mCherry* mice were interbred with $Lyzm^{Cre}$ mice to generate offspring that express *DTR* in $Lyz2^+Csf1r^+$ cells (MM^{DTR} mice) (Schreiber et al., 2013). BALB/c mice (no. 028) were obtained from Charles River Laboratories. Mice lacking both *Lxr-α* and *Lxr-β* (LXR^{DKO}) on C57BL/6 background were generously provided by David Mangelsdorf (UT Southwestern Medical Center, Dallas, TX, USA). $OT\text{-}I^{Lxr\text{-}DKO}$ were generated by crossing OT-I mice with LXR^{DKO} mice.

Mouse genotyping

All mouse strains were genotyped according to standard protocols as recommended by The Jackson Laboratory.

Cell lines

E0771 cells were purchased from CH3 BioSystems. Lewis lung carcinoma (LLC), B16F10 melanoma, and CT26 colon cancer cells were obtained from American Tissue Type Collection. All cell lines were cultured according to the suppliers' recommendations. Mycoplasma contamination was ruled out by intermittent PCR-based testing according to standard protocols.

Generation of reporter and highly metastatic cell lines

Standard cloning techniques were employed to generate a lentiviral expression vector encoding Luciferase and mCherry (dual reporter vector, DR). Briefly, a sequence coding for an internal ribosomal reentry site (IRES) and mCherry was amplified from a pMX-IRES-mCherry vector (a kind gift of M.C. Nussenzweig,

The Rockefeller University, New York City, NY, USA) by PCR using the primers 5′-TAAGCAGGATCCCCCCTCTCCCTCCCC CCC-3′ and 5′-TGCTTAATCGATTTACTTGTACAGCTCGTCCAT GCC-3′. The PCR product was then subcloned into the expression vector pHIV-Luciferase-zsGreen (Addgene plasmid no. 39196) using the restriction enzymes BamHI and ClaI (New England Biolabs) to replace zsGreen with mCherry. Similarly, a lentiviral expression vector encoding a cytosolic form of OVA and mCherry was generated (pHIV-cOVA-mCherry, cOC). Specifically, fragments of chicken OVA excluding its signal sequence (full-length sequence as in Addgene plasmid #64599, synthesized by GeneArt) were amplified using the primers 5′-TAAGCAGCGGCCGCTGAACTGGAA-3′ and 5′-TACCCAGGA ATTGATGAGCTCCTTGAATACATCAAAACA-3′ to amplify the N-terminal portion, as well as primers 5′-GTATTCAAGGAG CTCATCAATTCCTGGGTAGAA-3′ and 5′-GCTTATCTAGAT TAAGGGGAAACACATCTGCC-3′ to amplify the C-terminal portion. Subsequently, these amplicons were fused by overlap extension PCR yielding the coding sequence for cytoplasmatically retained OVA and subsequently shuttled into the DR vector using the restriction enzymes NotI and XbaI (NEB Biolabs) to replace luciferase.

To generate E0771-DR and E0771-cOC cell lines, lentivirus production and target cell transduction were performed according to standard protocols using a third-generation lentiviral system (Cell Biolabs) as described previously (Nguyen et al., 2016). mCherry-positive cells were sorted on a FACS Aria II (BD Biosciences). To generate E0771-LM1-DR cells with enhanced lung metastatic capacity, 5 × 10^5 E0771-DR cells resuspended in PBS were injected into a C57BL/6J mouse by tail vein. Upon developing pronounced bioluminescence signal, the lungs were resected on day 16 after injection, finely minced using scalpels, red blood cells were lysed in ACK lysis buffer (Lonza), and tissue pieces were digested with 1.25 mg/ml Collagenase I (Worthington Biochemical Corp.) in HBSS (14020; Gibco) supplemented with 2% FBS, 25 mM HEPES (15630; Gibco), and 1 mM sodium pyruvate (11360; Gibco) for 1 h at 37°C on an orbital shaker at 220 rpm. Subsequently, another digestion step in 0.25% trypsin was completed for 10 min at 37°C before plating the cells in complete growth medium. After two passages, mCherry$^+$ cells were repurified on a FACS Aria II (BD Biosciences).

Tumor growth studies

For all tumor growth studies, 6–10 wk old, age-matched mice were used. Female mice were used for breast cancer studies (E0771), and male mice were used for experiments with LLC, B16F10 melanoma, and CT26 colon cancer cells. Tumor cells were mixed 1:1 with growth factor reduced Matrigel (356231; Corning) before injection in a total volume of 100 µl. The following cell numbers were injected: 1 × 10^5 cells for unlabeled E0771, Lewis lung carcinoma, and B16F10 models; 2 × 10^5 cells for E0771-DR, E0771-cOC, and CT26 models. Where indicated, E0771 cells were orthotopically injected into the fourth mammary fat pad of mice via a small surgical incision and direct injection into the fat pad. For all other primary tumor growth studies, cells were injected subcutaneously into the flank.

LXR-agonistic treatment in vivo

Unless indicated otherwise, in vivo treatment with the synthetic LXR agonist RGX-104 (Tavazoie et al., 2018) was initiated on day 3 after tumor cell injection at a target dose of 100 mg/kg (rodent chow supplemented with RGX-104 at 628.5 mg per kg chow, Research Diets).

Radiation therapy

Mice as indicated in the figures were irradiated on days 7 and 19 after tumor cell injection with two gray whole-body irradiation using an RS 2000 irradiator (Rad Source).

RGX-104 and anti-CD40 combination therapy

Mice were treated with RGX-104 starting on day 3 after injection of 100,000 E0771 cells into the mammary fat pad (mixed 1:1 with growth factor reduced Matrigel as outlined above). In addition, mice received 200 µg of either IgG2A control antibody (BioXcell, clone 2A3) or anti-CD40 antibody (BioXcell, clone FGK4.5) by intraperitoneal injection on day 5 after injection and 100 µg of either antibody on days 8, 11, 14, and 17 after injection.

Experimental metastasis

For experimental metastasis assays, cells were resuspended in PBS and strained twice through a 40-µm cell strainer. Subsequently, 100 µl containing 1 × 10^5 E0771 or E0771-LM1-DR cells were injected into the tail vein. For luciferase-labeled cell lines, metastatic progression was monitored via noninvasive bioluminescence imaging using D-luciferin substrate (Perkin Elmer) as described previously (Pencheva et al., 2012).

Tumor rechallenge

LXR agonistic treatment was terminated ∼2 wk after last palpable tumor measurement in mice that had cleared primary orthotopic E0771-DR tumors. Approximately 2 mo later, mice were rechallenged with unlabeled E0771 cells. For primary tumor rechallenge, mice were injected with orthotopic mammary fat pad tumors as outlined above on the contralateral side of the original tumor. For metastatic rechallenge, mice were injected with 1 × 10^5 unlabeled E0771 cells resuspended in PBS by tail vein injection. Naïve mice served as controls for both primary tumor and metastatic rechallenge.

Immunofluorescence staining

For staining of tumor-resident CD8$^+$ T cells, tumors were resected, embedded in OCT compound (4583; VWR), and snap-frozen. Slides were incubated with ice-cool acetone, a 1:1 mix of acetone/methanol, and acetone again at −20°C for 5 min each before washing with PBS with 0.1% Tween-20 (PBST) and incubation with 5% goat serum in PBST for 30 min. Sections were then incubated with primary antibody (rabbit anti-CD8, clone EPR21769; Abcam, 1:500 dilution) overnight at 4°C. The next day, slides were washed three times with PBST for 5 min each, incubated with secondary antibody (goat anti-rabbit AF488-conjugated, 1:200 dilution, Thermo Fisher Scientific) and DAPI (1 µg/ml, Roche) for 45 min at room temperature. After subsequent washes, slides were mounted with Prolong Gold (Thermo Fisher Scientific), and images were acquired with a Nikon A1R confocal microscope (20× magnification) using Nikon NIS

elements software (version 5.20.02). For quantification of CD8⁺ T cells, we used CellProfiler (version 4.2.1) and averaged four images for each sample.

In vivo depletion of CD8⁺ cells

For depletion of CD8⁺ T cells, mice were injected with 250 µg anti-CD8 antibody (clone YTS 169.4; BioXcell) versus IgG control antibody (clone LTF-2; BioXcell) in a volume of 200 µl intraperitoneally on days 8, 11, and 14 after tumor cell injection.

Hematopoietic stem cell transplantation

Hematopoietic stem cell transplantation was performed as described recently (Ostendorf et al., 2020). In brief, 6–7-wk-old C57BL/6J recipient mice were whole-body irradiated with 10.5 gray (two doses of 525 rad each, 3.5 h apart; Rad Source, RS 2000 irradiator). Bone marrow cells were flushed from the tibia and femur bones of approximately 6–8 wk-old donor mice, passed through a 70-µm strainer, and 2–3 × 10^6 nucleated bone marrow cells were infused into recipient mice by retro-orbital injection. Transplanted mice were left for bone marrow reconstitution for at least 6 wk before experimental use.

In vivo depletion of DTR-expressing cells

For depletion of DTR-expressing hematopoietic cells, C57BL6/J mice transplanted with *CD11c*^{DTR} or *MM*^{DTR} bone marrow were intraperitoneally injected with an initial dose of 500 ng DT in 200 µl PBS (D0564; Sigma-Aldrich) on day 3 after tumor injection. Afterward, mice were injected with 150 ng (*CD11c*^{DTR}) or 200 ng (*MM*^{DTR}) DT every other day to maintain depletion. Control mice received PBS injections.

Isolation of LN-resident and tumor-infiltrating leukocytes

Tumor-infiltrating leukocytes were isolated as described recently (Ostendorf et al., 2020). Briefly, tumors were resected on day 9 (analysis of myeloid and T cells in DLN and of myeloid cells in tumors) or day 11 (analysis of T cells in tumors) after injection and finely minced using scalpels. Tumor pieces were digested in HBSS2⁺ (HBSS with calcium and magnesium [24020; Gibco] supplemented with 2% FBS, 1 mM sodium pyruvate [11360; Gibco], 25 mM HEPES [15630; Gibco], 500 U/ml Collagenase IV [LS004188; Worthington], 100 U/ml Collagenase I [LS004196; Worthington], and 0.2 mg/ml DNAse I [10104159001; Roche]) for 30 min on an orbital shaker (80 rpm) at 37°C, triturated, and then passed through a 70-µm strainer. Leukocytes were enriched at the interphase of 35%/70% Percoll phases by density gradient centrifugation (20 min at 800 × *g* at room temperature without brakes) and washed twice in HBSS2 (HBSS without calcium and magnesium [14170; Gibco], 2% FBS, 1 mM sodium pyruvate, and 25 mM HEPES). LN-resident leukocytes were isolated similarly except for omitting density gradient centrifugation.

Generation of BMDCs

For generation of BMDCs, bone marrow cells were flushed from tibias and femurs of 6–10-wk-old C57BL6 or C57BL6 LXR^{DKO} mice and passed through a 70-µm strainer. Red blood cells were lysed by incubation in hypotonic ACK buffer (10-548E; Lonza) for 3–5 min. Bone marrow cells were plated at 2.5 × 10^6/ml in RPMI supplemented with 10% FBS, nonessential amino acids (11140-050; Thermo Fisher Scientific), 500 µM β-mercaptoethanol (194705; MP Biomedicals), and 300 ng/ml recombinant Flt3l (550704; BioLegend) and left to differentiate for 7 days.

In vitro LXR-agonistic treatment of DCs

BMDCs were generated as described above, harvested on day 7 of culture by gently resuspension, and 50,000 BMDCs per well were plated on 96-well plates. Cells were treated with 2 µM RGX-104 versus DMSO for 24 h and subsequently analyzed by flow cytometry as described below.

Isolation and culture of CD8⁺ cells

Spleens and LNs of 6–10-wk-old OT-I, OT-I LXR^{DKO}, or wild-type C57BL6 mice as indicated in the figures were resected and minced using scalpels. Tissue chunks were vigorously resuspended in HBSS2 and strained using a 70-µm strainer. Red blood cells were lysed by incubation for 5 min in ACK buffer (10-548E; Lonza). Cells were then washed and strained again. CD8⁺ T cells were isolated using the CD8a⁺ T cell isolation kit (130-104-075; Miltenyi) according to the manufacturer's instructions. For treatment of naïve CD8⁺ T cells in isolation, the MojoSort Mouse CD8 Naïve T Cell Isolation Kit (BioLegend; 480044) was used according to the manufacturer's instructions. T cells were cultured in RPMI supplemented with 10% FBS, penicillin/streptomycin (15140; Gibco), 2 mM L-glutamine (25030; Gibco), 1 mM sodium pyruvate (11360070; Gibco), amino acids (11130; Gibco), 25 mM HEPES (15630; Gibco), 500 µM β-mercaptoethanol (194705; MP Biomedicals), and 40 U/ml IL-2 (200-02-500; PeproTech).

In vitro cross-presentation and T cell activation assays

BMDCs generated as described above were harvested by gently resuspending, incubated in BMDC medium supplemented with 500 ng/ml SIINFEKL peptide (Rockefeller University proteomics core facility) for 2 h, and washed in 50 ml PBS. 5,000 BMDCs and 30,000 labeled CD8⁺ OT-I T cells per well were plated on a 96-well plate. For drug treatment, RGX-104 was added at a final concentration of 2 µM, and carrier (DMSO) was used as control. Three hours before harvest, Brefeldin A (420601; BioLegend) was added to a final concentration of 5 µg/ml. Finally, flow cytometry was performed after 24 h of co-culture as described below.

For assessing the impact of LXR activation on T cells stimulated in isolation, 50,000 naïve CD8⁺ T cells per well were stimulated for 24 h on anti-CD3 (clone 17A2; BioLegend) and anti-CD28 (clone 37.51; BioLegend)-coated plates. 96-well plates were coated by incubating wells with 50 µl sterile water containing 1 µg/ml anti-CD3 and 3 µg/ml anti-CD28 for 10 h at 4°C; plates were subsequently washed with PBS twice. We assessed the impact of LXR agonism on T cell activation at different times relative to anti-CD3/CD28-mediated stimulation. To assess the impact of LXR activation simultaneous with anti-CD3/CD28 treatment, cells were either directly cultured on anti-CD3/anti-CD28–coated plates with simultaneous treatment with RGX-104 at a final concentration of 2 µM versus carrier (DMSO) (simultaneous early condition) or first cultured for 24 h before subsequent treatment and stimulation (simultaneous late condition). For assessing the impact of LXR activation prior to stimulation,

cells were cultured first in a 96-well plate and treated with RGX-104 or DMSO for 24 h. CD8⁺ T cells were then harvested and washed in 50 ml PBS to remove the compound. 50,000 T cells were resuspended in fresh T cell medium and plated on anti-CD3/anti-CD28–coated plates for 24 h stimulation before reading out by flow cytometry. When culturing T cells with LXR agonist/DMSO prior to or entirely in absence of CD3/CD28 ligation, 10 ng/ml IL-7 (217-17; PeproTech) was added to the medium to maintain high cell viability in the absence of stimulation. Cells were stained and analyzed by flow cytometry as described below. Three hours before harvest, Brefeldin A (420601; BioLegend) was added to a final concentration of 5 µg/ml.

Flow cytometry

Flow cytometry assays were performed as described previously (Ostendorf et al., 2020). In brief, all steps were performed on ice under protection from light, unless noted otherwise. Fc receptors on leukocytes isolated from tumors or tumor DLNs as described above were blocked by incubation with 2.5 µg/ml anti-CD16/32 antibody (clone 93; 101320; BioLegend) in staining buffer (25 mM HEPES, 2% FBS, 10 mM EDTA [351-027; Quality Biological], and 0.1% sodium azide [7144.8-16; Ricca] in PBS) for 10 min. Subsequently, cells were stained with antibodies diluted in staining buffer for 20 min, washed with PBS, incubated with Zombie NIR Fixable Live/Dead Stain (423105; BioLegend) for 20 min at room temperature, and washed twice with staining buffer. Subsequent analysis was performed on an LSRFortessa (BD Biosciences).

To stain intracellular cytokines, cells were restimulated with 500 ng/ml ionomycin (I0634; Sigma-Aldrich), 100 ng/ml phorbol 12-myristate 13-acetate (P8139; Sigma-Aldrich), and 10 µg/ml brefeldin A (B7651; Sigma-Aldrich) for 3 h at 37°C. Surface antigens were then labeled, and live/dead staining was performed as described above before incubation in fixation/permeabilization buffer (00-5523; eBioscience) for 30 min. After subsequent washing with permeabilization buffer (00-5523; eBioscience), intracellular antigens were labeled with antibodies diluted in permeabilization buffer for 20 min. Cells were then washed first with permeabilization buffer and finally with staining buffer.

Antibodies

The following anti-mouse, fluorophore-conjugated antibodies were used for flow cytometry: CD45 (clone 30-F11; BioLegend), B220 (clone RA3-6B2; BD Biosciences), CD4 (clone GK1.5; BioLegend), CD8α (clone 53-6.7; BioLegend), CD11b (clone M1/70; BioLegend), CD11c (N418; BioLegend), CD19 (clone 1D3/CD19; BioLegend), CD24 (clone M1/69; BioLegend), CD40 (2/23; BioLegend), CD86 (PO3; BioLegend), CD44 (IM7; BioLegend), CD62L (MEL-14; BioLegend), CD69 (H1.2F3; BioLegend), CD103 (clone 2E7; BioLegend), Ly6G (clone 1A8; BD Biosciences), Ly6C (clone HK1.4; BioLegend), I-A/I-E (clone M5/11.15.2; BioLegend), F4/80 (clone BM8; BioLegend), TCRβ (clone H57-957; BioLegend), Foxp3 (FJK-16 s; eBioscience), TNFα (MP6-XT22; BioLegend), Granzyme B (clone QA16A02; BioLegend), and IFNγ (clone XMG1.2; BioLegend).

Transcriptomic profiling of CD8⁺ T cells

For transcriptomic profiling of CD8⁺ OT-I T cells after co-culture with BMDCs, cross-presentation assays were performed as outlined above. 19 h after start of the co-culture, cells were stained for flow cytometry as described above, and CD8⁺DAPI⁻ T cells were sorted using a FACSAria sorter (BD Biosciences). RNA from 100,000 cells was extracted using the Total RNA isolation kit from Norgen (17200; Norgen) including the DNAse digest. Sequencing libraries were prepared with the Quantseq 3′ mRNA-Seq Library Prep kit (113.96; Lexogen) using 500 ng as input, and libraries were sequenced on an Illumina NextSeq 500 sequencer. Bioinformatic analysis was performed similarly as described previously (Ostendorf et al., 2022). In brief, polyA sequences and adapters were trimmed using BBDuk (version 38.9, options k = 13, ktrim = r, forcetrimleft = 11, useshortkmers = t, mink = 5, qtrim = t, trimq = 10, and minlength = 20). Reads were aligned to the mm10 mouse Genome using STAR (version 2.7.8a) at default settings except for "outFilterMismatchNoverReadLmax 0.1." Reads were counted with STAR using "--quantMode GeneCounts." Downstream processing was performed using R (version 4.1) with the DESeq2 package (version 1.40). Normalized and $\log_2$-transformed counts were plotted using the aheatmap function from the NMF package (version 0.26).

For profiling of CD8⁺ OT-I T cells after co-culture with *LXR*^{DKO} BMDCs, the same steps as above were followed except for using the TruSeq library preparation kit (RS-122-2001; Illumina), trimming adapters using Cutadapt (version 2.10), and counting reads using STAR (version 2.7.5c).

For profiling of naïve CD8⁺ T cells after 24 h of LXR activation in the absence of CD3/CD28 ligation, we isolated RNA from 60,000 cells per replicate using the Monarch Total RNA extraction kit (T20105; Biolabs) according to the manufacturer's instructions. Subsequently, we used 1.3 ng per samples as input to the Quantseq 3′ mRNA-Seq Library Prep kit (113.96; Lexogen) according to the manufacturer's instructions and adhering to low-input protocol modifications. Subsequent bioinformatic analyses were performed as outlined above for the analysis of CD8⁺ OT-I T cells after BMDC co-culture.

Chromatin accessibility profiling of T cells

For assay for transposase-accessible chromatin with sequencing (ATAC-seq), previously published protocols were largely followed (Buenrostro et al., 2015; Corces et al., 2017). T cells were prepared as outlined above for the transcriptomic profiling of CD8⁺ OT-I T cells. In brief, biological duplicates of 60,000 sorted T cells were pelleted in 1 ml of cold PBS (500 *g*, 5 min), and the pellet was resuspended in lysis buffer (0.1% IGEPAL CA-630, 0.1% Tween-20, and 0.01% digitonin; diluted in resuspension buffer: 10 mM Tris-HCl, 10 mM NaCl, and 3 mM $MgCl_2$), incubated for 3 min on ice, and washed with resuspension buffer. Cell pellets were then resuspended in 50 µl transposition reaction mix (1× Tagment DNA buffer, 0.1% Tween-20, 0.01% digitonin, and 2.5 µl Tn5 Transposase [Illumina, Tagment DNA Enzyme 1] in PBS) and incubated at 37°C for 30 min on a thermomixer (1,000 rpm). Transposed DNA fragments were amplified in a 50 µl reaction (1.25 µM of each forward and reverse primer [primer sequences listed below], 10 µl transposed DNA, and 1× NEBNext High-Fidelity PCR Master Mix [M0541; New England Biolabs]) with one cycle of 72°C for 5 min and 98°C for 30 s, followed by 12 cycles of 98°C for 10 s, 63°C for 30 s, and 72°C

for 1 min. Libraries were cleaned using AMPure XP beads (A63880; Beckman) and sequenced on a NextSeq 500 sequencer (Illumina; 2 × 40 bp PE).

ATAC-seq forward primer: 5′-AATGATACGGCGACCACC GAGATCTACACTCGTCGGCAGCGTCAGATGTG-3′

ATAC-seq reverse primer #1: 5′-CAAGCAGAAGACGGCATA CGAGATTCGCCTTAGTCTCGTGGGCTCGGAGATGT-3′

ATAC-seq reverse primer #2: 5′-CAAGCAGAAGACGGCATA CGAGATCTAGTACGGTCTCGTGGGCTCGGAGATGT-3′

ATAC-seq reverse primer #3: 5′-CAAGCAGAAGACGGCATA CGAGATTTCTGCCTGTCTCGTGGGCTCGGAGATGT-3′

ATAC-seq reverse primer #4: 5′-CAAGCAGAAGACGGCATA CGAGATGCTCAGGAGTCTCGTGGGCTCGGAGATGT-3′

For downstream analysis, reads were trimmed using Cutadapt PE (version 2.10) using "-g AATGATACGGCGACCACCGAGATC TACACTCTTTCCCTACACGACGCTCTTCCGATCT" and mapped to the GRCm38 reference using BWA (version 0.7.17) at default settings. PCR duplicates were marked using Picard (version 2.22.1). Unstructured genomic regions as previously defined (Amemiya et al., 2019) were filtered using the "intersect" function from bedtools (version 2.3), and unmapped, low-quality, and duplicated reads were filtered using the "view" function from samtools (version 1.10) with the settings "-b -h -q 30 -F 0x004 -F 0x0400 -G 0x009 -f 0x001." Subsequently, reads mapping to chromosome M were filtered, and bigwig files were generated using the "bamCoverage" function from deepTools (version 3.5.1) (settings "--binSize 10 --normalizeUsing RPGC --effectiveGenomeSize 2150570000 –extendReads"). narrowPeaks and bed files were generated using Genrich (version 0.6.1) using the parameters "-vjr -m 30," and differential peak analysis was performed using Diffbind (version 3.10). Analysis for the enrichment of transcription factor–binding motifs in differentially accessible peaks was performed using the memes package (version 1.8.0).

For chromatin accessibility profiling of naïve CD8⁺ T cells, we used 60,000 cells per replicate as input for the ATAC-Seq kit (53150; Active Motif) according to the manufacturer's instructions. Subsequent bioinformatic analyses were performed as outlined above for the analysis of CD8⁺ OT-I T cells after BMDC co-culture.

CUT&Tag profiling

CUT&TAG was performed as previously described (Kaya-Okur et al., 2019). Approximately 50,000 cells were resuspended in Nuclear Extraction (NE) Buffer (20 mM HEPES-KOH, pH 7.9, 10 KCl, 0.1% Triton X-100, 20% glycerol, 0.5 mM spermidine, and cOmplete protease inhibitor) and incubated on ice for 10 min. Nuclei were pelleted by centrifugation for 3 min at 600 × *g*, resuspended in 100 µl NE buffer with 10 µl of concanavalin A–conjugated paramagnetic beads (Bangs Laboratories), and incubated for 10 min at room temperature. Supernatant was discarded, and beads were resuspended in 50 ml of antibody buffer (20 mM HEPES, pH 7.5, 150 NaCl, 0.5 mM spermidine, 0.01% digitonin, 2 mM EDTA, and cOmplete protease inhibitor) containing 0.5 mg mouse IgG or anti-LXRb (Thermo Fisher Scientific) antibody. Samples were incubated overnight at 4° and resuspended in 50 ml of digitonin buffer (20 mM HEPES, pH 7.5, 150 NaCl, 0.5 mM spermidine, 0.01% digitonin, and cOmplete protease inhibitor) containing 0.5 mg of rabbit Secondary Antibody (EpiCypher). After 30-min incubation at room temperature, beads were washed twice with digitonin buffer and resuspended in 50 ml of digitonin buffer with 300 mM NaCl + 2.5 ml of CUTANA pAG-Tn5 (EpiCypher). Reactions were incubated for 1 h at room temperature, washed twice with digitonin buffer, resuspended in 50 ml of tagmentation buffer (20 mM HEPES, pH 7.5, 300 NaCl, 10 mM $MgCl_2$, 0.5 mM spermidine, 0.01% digitonin, and cOmplete protease inhibitor), and placed in a thermocycler for 1 h at 37°. Supernatant was discarded, beads were washed with TAPS buffer (10 mM TAPS pH 8.5, and 0.2 mM EDTA), and incubated at 58° for 1 h in 5 ml SDS buffer (10 mM TAPS, pH 8.5, and 0.1% SDS). 15 ml of a 0.67% Triton X-100 solution was then added to quench reactions, and PCR amplification was performed using i5 and i7 barcoded primers, followed by DNA cleanup using AMPure beads (Beckman Coulter). Paired-end sequencing was carried out using an Illumina Novaseq instrument. Reads were trimmed using Trimmomatic v.0.39, fastq files were aligned to the mm10 genome using Bowtie2, and peaks were called using MACS2. Gene tracks were generated using the UCSC Genome Browser Custom Tracks feature.

scRNAseq and TCRseq

Female C57BL6/J mice (n = 8 per group) were subcutaneously injected in the lateral flank with 200,000 E0771-DR cells and treated with control chow versus RGX-104–containing chow from day 3 after, as described above. Tumor DLNs were harvested 8 days after injection, processed to generate single-cell suspensions, and stained for flow cytometric sorting as outlined above. Subsequently, 9,000 DAPI⁻CD45⁺B220⁻CD90⁺ T cells and 4,000 DAPI⁻CD45⁺CD90⁻B220⁻NK1.1⁻Ly6G⁻ and CD11b⁺ or CD11c⁺ APCs from each mouse were independently sorted on a BD FACSAria II cell sorter, and cells from the same condition were pooled (i.e., total of 104,000 cells; representative gating shown in Fig. S2 g). For each condition, 8,000 cells were targeted for scRNAseq and TCRseq on a Chromium Single Cell System (10x Genomics). Libraries were generated using the 10x Genomics 5′ scRNAseq and VDJ kits according to the manufacturer's instructions and sequenced on an Illumina NovaSeq SP sequencer.

To generate transcript matrices, sequencing results were preprocessed using the 10x Genomics cell ranger pipeline at default settings (version 5.0.0). Subsequent downstream analysis was performed in R using the Seurat package (version 5.0.3). Cells were removed from analysis if <800 or >6,000 unique features were detected, if mitochondrial transcripts contributed to >5% of reads, or if cells were identified as likely doublets using the "scDblFinder" function from the scDblFinder package (version 1.18.0). Datasets from the two conditions were integrated using RPCA-based integration. Data were scaled, and principal component analysis was performed using Seurat's default settings, except for regressing out proliferation-associated genes using Seurat's "CellCycleScoring" function. For clustering of cells, the "FindNeighbors" and "FindClusters" functions were used at default settings; for visualization of clusters, uniform manifold approximation and projection (UMAP) was calculated with the "RunUMAP function" with "dims" set to 15. Subsequently,

clusters containing either APCs or T cells were subset based on expression of canonical markers (*Itgax* and *Flt3* for APCs; *CD3e* for T cells).

The subset containing APCs was re-clustered using Seurat's "FindUMAP," FindNeighbors (each with dims set to 20) and FindClusters (resolution: 0.5) functions, and top differentially expressed genes were cross-referenced with the Immunological Genomics Project (Yoshida et al., 2019) and previous studies (Binnewies et al., 2019; Rodrigues et al., 2023) to determine cluster identities. Specifically, cytotoxic T cells were identified given their high expression of genes encoding effector molecules including *Gzma*, *Prf1*, and *Gzmk*; T helper cells were differentiated from $CD8^+$ T cells based on the expression of *Cd4* and *Cd8*, respectively; Tregs showed highest expression of *Foxp3*, and γδ-T cells were identified based on their uniquely high expression of *Sox13* and *Il17re* (Fig. S2, k and l).

The subset containing T cells was similarly re-clustered, except for setting "resolution" to 1.2 in the FindClusters function. Cluster identity was determined by again cross-referencing top differentially expressed genes with the Immunological Genomics Project. The scRNAseq transcriptional profiling dataset was merged with the TCRseq data using the "combineExpression" function from the "scRepertoire" package (version 2.0.0). scRepertoire was also used to determine clonality, and T cells were marked as "expanded" if the given clonotype was identified more than once.

Clinical data

Whole blood was drawn in PAXgene DNA tubes from patients participating in a phase 1 trial, NCT02922764 at pre-dose, and either cycle 2 day 1 or cycle 3 day 1 for the post-treatment time point. Frozen specimens were shipped to Adaptive Biotechnologies where samples were processed using proprietary methods for deep sequencing of the CDR3 regions of the TCRβ locus using a multiplex PCR amplification across the VDJ junction of rearranged TCR. Approximately 6–25 µg of genomic DNA was used for analysis. The protocol was approved by the WIRB-Copernicus Group (WCG) institutional review board and patients signed informed consent before any screening procedures were obtained.

Statistical analysis

Unless otherwise noted, all data points shown represent biological replicates with dots referring to individual mice. Bars represent mean values with error bars representing ± standard error of the mean. Statistical testing for significant differences between groups was performed as indicated in the figure legends and text. A significant difference was concluded at $P < 0.05$. Throughout all figures: *$P < 0.05$, **$P < 0.01$, ***$P < 0.001$, and ****$P < 0.0001$.

Online supplemental material

Fig. S1 shows gating strategies and further results of flow cytometric immunophenotyping of tumors from control versus RGX-104–treated mice. Fig. S2 shows gating strategies and flow cytometric and scRNAseq results of tumor DLN-resident T cells and APCs. Fig. S3 shows gating strategies and flow cytometric profiling of APCs in tumors from control versus RGX-104–treated mice as well as scRNAseq results of tumor DLN-resident APCs. Fig. S4 shows flow cytometric profiling of APCs and T cells in tumor DLNs from wild-type versus *Apoe*-KO mice and tumor progression in wild-type versus *Cd1d*-KO and in mice transplanted with wild-type versus *Ldlr*-KO bone marrow. Fig. S5 shows gating strategies and further profiling results of T cells co-cultured with DCs and treated with RGX-104.

Data availability

Bulk transcriptomic and chromatin accessibility data as well as scRNAseq/TCRseq data have been deposited at the Gene Expression Omnibus database (accession numbers GSE249947 and GSE275714, respectively). Code is publicly available at https://github.com/benostendorf/ostendorf_etal_2026.

Acknowledgments

We are grateful to members of the Tavazoie and Ostendorf labs for comments on previous versions of the manuscript. We thank Svetlana Mazel and staff and Connie Zhao and staff at the Rockefeller University flow cytometry and genomics resource centers, respectively, for assistance with data collection and analysis. We thank Vaughn Francis and other veterinary staff at the Comparative Bioscience Center for animal husbandry. At Charite University Medicine, we thank Janine Altmueller and staff and Desiree Kunkel and staff at the genomics and flow cytometry resource centers, respectively, for assistance with data collection and analysis.

S.F. Tavazoie was supported by grants from the National Cancer Institute of the National Institutes of Health under award numbers R35CA274446 and U54CA261701 as well as the Black Family Metastasis Center. B.N. Ostendorf was supported by a Deutsche Forschungsgemeinschaft postdoctoral fellowship (OS 498/1-1), by a Max Eder grant of the German Cancer Aid (reference 70114327), by a grant of the Thyssen foundation (reference 10.24.1.010MN), by a fellowship of the Charité-BIH Digital Clinician Scientist Program and by a scholarship of the Advanced Clinician Scientist Program of the German Society of Internal Medicine. J.G. Goldstein was supported by a Boehringer Ingelheim Foundation MD fellowship. S. Liu was supported by a scholarship from the Guangzhou Elite Project (JY202217). J. Bilanovic, M. Yuan, and J.Y. Kim were supported by scholarships of the German National Academic Foundation.

Author contributions: Benjamin N. Ostendorf: conceptualization, data curation, formal analysis, funding acquisition, investigation, methodology, project administration, resources, software, supervision, validation, visualization, and writing—original draft, review, and editing. Jonathan G. Goldstein: formal analysis, investigation, validation, visualization, and writing—review and editing. Shuang Liu: investigation. Foster C. Gonsalves: conceptualization, data curation, formal analysis, investigation, methodology, project administration, supervision, and writing—review and editing. Jana Bilanovic: investigation. Mathias Yuan: investigation. Ji-Young Kim: investigation. Christopher Rouya: formal analysis and investigation. Masoud Tavazoie: conceptualization,

supervision, and writing—review and editing. Sohail F. Tavazoie: conceptualization, data curation, formal analysis, funding acquisition, investigation, methodology, project administration, resources, supervision, and writing—original draft, review, and editing.

Disclosures: M.Tavazoie reported personal fees from Inspirna during the conduct of the study. S.F. Tavazoie reported personal fees from Inspirna outside the submitted work; in addition, S.F. Tavazoie had a patent number 9,399,028 licensed (Inspirna). No other disclosures were reported.

Submitted: 3 November 2025
Revised: 21 December 2025
Accepted: 13 January 2026

References

Amemiya, H.M., A. Kundaje, and A.P. Boyle. 2019. The ENCODE blacklist: Identification of problematic regions of the genome. *Sci. Rep.* 9:9354. https://doi.org/10.1038/s41598-019-45839-z

Armstrong, A.J., A.K. Gebre, J.S. Parks, and C.C. Hedrick. 2010. ATP-binding cassette transporter G1 negatively regulates thymocyte and peripheral lymphocyte proliferation. *J. Immunol.* 184:173–183. https://doi.org/10.4049/jimmunol.0902372

Beceiro, S., A. Pap, Z. Czimmerer, T. Sallam, J.A. Guillén, G. Gallardo, C. Hong, N. A-Gonzalez, C. Tabraue, M. Diaz, et al. 2018. LXR nuclear receptors are transcriptional regulators of dendritic cell chemotaxis. *Mol. Cell Biol.* 38:e00534-17. https://doi.org/10.1128/MCB.00534-17

Bensinger, S.J., M.N. Bradley, S.B. Joseph, N. Zelcer, E.M. Janssen, M.A. Hausner, R. Shih, J.S. Parks, P.A. Edwards, B.D. Jamieson, and P. Tontonoz. 2008. LXR signaling couples sterol metabolism to proliferation in the acquired immune response. *Cell*. 134:97–111. https://doi.org/10.1016/j.cell.2008.04.052

Binnewies, M., A.M. Mujal, J.L. Pollack, A.J. Combes, E.A. Hardison, K.C. Barry, J. Tsui, M.K. Ruhland, K. Kersten, M.A. Abushawish, et al. 2019. Unleashing type-2 dendritic cells to drive protective antitumor CD4+ T cell immunity. *Cell*. 177:556–571.e16. https://doi.org/10.1016/j.cell.2019.02.005

Bosteels, V., S. Maréchal, C. De Nolf, S. Rennen, J. Maelfait, S.J. Tavernier, J. Vetters, E. Van De Velde, F. Fayazpour, K. Deswarte, et al. 2023. LXR signaling controls homeostatic dendritic cell maturation. *Sci. Immunol.* 8:eadd3955. https://doi.org/10.1126/sciimmunol.add3955

Broz, M.L., M. Binnewies, B. Boldajipour, A.E. Nelson, J.L. Pollack, D.J. Erle, A. Barczak, M.D. Rosenblum, A. Daud, D.L. Barber, et al. 2014. Dissecting the tumor myeloid compartment reveals rare activating antigen-presenting cells critical for T cell immunity. *Cancer Cell*. 26:638–652. https://doi.org/10.1016/j.ccell.2014.09.007

Buenrostro, J.D., B. Wu, H.Y. Chang, and W.J. Greenleaf. 2015. ATAC-seq: A method for assaying chromatin accessibility genome-wide. *Curr. Protoc. Mol. Biol.* 109:21.29.1–21.29.9. https://doi.org/10.1002/0471142727.mb2129s109

Candelaria, N.R., S. Addanki, J. Zheng, T. Nguyen-Vu, H. Karaboga, P. Dey, C. Gabbi, L.-L. Vedin, K. Liu, W. Wu, et al. 2014. Antiproliferative effects and mechanisms of liver X receptor ligands in pancreatic ductal adenocarcinoma cells. *PLoS One*. 9:e106289. https://doi.org/10.1371/journal.pone.0106289

Carbo, J.M., T.E. León, J. Font-Díaz, J.V. De la Rosa, A. Castrillo, F.R. Picard, D. Staudenraus, M. Huber, L. Cedó, J.C. Escolà-Gil, et al. 2021. Pharmacologic activation of LXR alters the expression profile of tumor-associated macrophages and the abundance of regulatory T cells in the tumor microenvironment. *Cancer Res.* 81:968–985. https://doi.org/10.1158/0008-5472.CAN-19-3360

Chan, C.T., A.M. Fenn, N.K. Harder, J.E. Mindur, C.S. McAlpine, J. Patel, C. Valet, S. Rattik, Y. Iwamoto, S. He, et al. 2020. Liver X receptors are required for thymic resilience and T cell output. *J. Exp. Med.* 217:e20200318. https://doi.org/10.1084/jem.20200318

Chen, D.S., and I. Mellman. 2013. Oncology meets immunology: The cancer-immunity cycle. *Immunity*. 39:1–10. https://doi.org/10.1016/j.immuni.2013.07.012

Cheng, H.-Y., R. Wu, A.K. Gebre, R.N. Hanna, D.J. Smith, J.S. Parks, K. Ley, and C.C. Hedrick. 2013. Increased cholesterol content in gammadelta (γδ) T lymphocytes differentially regulates their activation. *PLoS One*. 8:e63746. https://doi.org/10.1371/journal.pone.0063746

Corces, M.R., A.E. Trevino, E.G. Hamilton, P.G. Greenside, N.A. Sinnott-Armstrong, S. Vesuna, A.T. Satpathy, A.J. Rubin, K.S. Montine, B. Wu, et al. 2017. An improved ATAC-seq protocol reduces background and enables interrogation of frozen tissues. *Nat. Methods*. 14:959–962. https://doi.org/10.1038/nmeth.4396

Elzen, P.V.D., S. Garg, L. León, M. Brigl, E.A. Leadbetter, J.E. Gumperz, C.C. Dascher, T.-Y. Cheng, F.M. Sacks, P.A. Illarionov, et al. 2005. Apolipoprotein-mediated pathways of lipid antigen presentation. *Nature*. 437:906–910. https://doi.org/10.1038/nature04001

Fukuchi, J., J.M. Kokontis, R.A. Hiipakka, C. Chuu, and S. Liao. 2004. Antiproliferative effect of liver X receptor agonists on LNCaP human prostate cancer cells. *Cancer Res.* 64:7686–7689. https://doi.org/10.1158/0008-5472.CAN-04-2332

Gabrilovich, D.I. 2017. Myeloid-derived suppressor cells. *Cancer Immunol. Res.* 5:3–8. https://doi.org/10.1158/2326-6066.CIR-16-0297

Goossens, P., J. Rodriguez-Vita, A. Etzerodt, M. Masse, O. Rastoin, V. Gouirand, T. Ulas, O. Papantonopoulou, M. Van Eck, N. Auphan-Anezin, et al. 2019. Membrane cholesterol efflux drives tumor-associated macrophage reprogramming and tumor progression. *Cell Metab.* 29:1376–1389.e4. https://doi.org/10.1016/j.cmet.2019.02.016

Guilbaud, E., T. Barouillet, M. Ilie, C. Borowczyk, S. Ivanov, V. Sarrazy, N. Vaillant, M. Ayrault, A. Castiglione, G. Rignol, et al. 2023. Cholesterol efflux pathways hinder KRAS-driven lung tumor progenitor cell expansion. *Cell Stem Cell*. 30:800–817.e9. https://doi.org/10.1016/j.stem.2023.05.005

Guo, D., F. Reinitz, M. Youssef, C. Hong, D. Nathanson, D. Akhavan, D. Kuga, A.N. Amzajerdi, H. Soto, S. Zhu, et al. 2011. An LXR agonist promotes glioblastoma cell death through inhibition of an EGFR/AKT/SREBP-1/LDLR–Dependent pathway. *Cancer Discov.* 1:442–456. https://doi.org/10.1158/2159-8290.CD-11-0102

Ito, A., C. Hong, K. Oka, J.V. Salazar, C. Diehl, J.L. Witztum, M. Diaz, A. Castrillo, S.J. Bensinger, L. Chan, and P. Tontonoz. 2016. Cholesterol accumulation in CD11c$^+$ immune cells is a causal and targetable factor in autoimmune disease. *Immunity*. 45:1311–1326. https://doi.org/10.1016/j.immuni.2016.11.008

Joseph, S.B., M.N. Bradley, A. Castrillo, K.W. Bruhn, P.A. Mak, L. Pei, J. Hogenesch, R.M. O'Connell, G. Cheng, E. Saez, et al. 2004. LXR-dependent gene expression is important for macrophage survival and the innate immune response. *Cell*. 119:299–309. https://doi.org/10.1016/j.cell.2004.09.032

Joseph, S.B., A. Castrillo, B.A. Laffitte, D.J. Mangelsdorf, and P. Tontonoz. 2003. Reciprocal regulation of inflammation and lipid metabolism by liver X receptors. *Nat. Med.* 9:213–219. https://doi.org/10.1038/nm820

Jung, S., D. Unutmaz, P. Wong, G. Sano, K. De los Santos, T. Sparwasser, S. Wu, S. Vuthoori, K. Ko, F. Zavala, et al. 2002. In vivo depletion of CD11c+ dendritic cells abrogates priming of CD8+ T cells by exogenous cell-associated antigens. *Immunity*. 17:211–220. https://doi.org/10.1016/s1074-7613(02)00365-5

Kaya-Okur, H.S., S.J. Wu, C.A. Codomo, E.S. Pledger, T.D. Bryson, J.G. Henikoff, K. Ahmad, and S. Henikoff. 2019. CUT&Tag for efficient epigenomic profiling of small samples and single cells. *Nat. Commun.* 10:1930. https://doi.org/10.1038/s41467-019-09982-5

Korf, H., S. Vander Beken, M. Romano, K.R. Steffensen, B. Stijlemans, J.A. Gustafsson, J. Grooten, and K. Huygen. 2009. Liver X receptors contribute to the protective immune response against Mycobacterium tuberculosis in mice. *J. Clin. Invest.* 119:1626–1637. https://doi.org/10.1172/JCI35288

Ma, X., E. Bi, Y. Lu, P. Su, C. Huang, L. Liu, Q. Wang, M. Yang, M.F. Kalady, J. Qian, et al. 2019. Cholesterol induces CD8+ T cell exhaustion in the tumor microenvironment. *Cell Metab.* 30:143–156.e5. https://doi.org/10.1016/j.cmet.2019.04.002

Maier, B., A.M. Leader, S.T. Chen, N. Tung, C. Chang, J. LeBerichel, A. Chudnovskiy, S. Maskey, L. Walker, J.P. Finnigan, et al. 2020. A conserved dendritic-cell regulatory program limits antitumour immunity. *Nature*. 580:257–262. https://doi.org/10.1038/s41586-020-2134-y

McGraw, J.M., F. Thelen, E.N. Hampton, N.E. Bruno, T.S. Young, W.L. Havran, and D.A. Witherden. 2021. JAML promotes CD8 and γδ T cell antitumor immunity and is a novel target for cancer immunotherapy. *J. Exp. Med.* 218:e20202644. https://doi.org/10.1084/jem.20202644

Michaels, A.J., C. Campbell, R. Bou-Puerto, and A.Y. Rudensky. 2020. Nuclear receptor LXRβ controls fitness and functionality of activated T cells. *J. Exp. Med.* 218:e20201311. https://doi.org/10.1084/jem.20201311

Nakajima, Y., K. Chamoto, T. Oura, and T. Honjo. 2021. Critical role of the CD44lowCD62Llow CD8+ T cell subset in restoring antitumor immunity in aged mice. *Proc. Natl. Acad. Sci. USA*. 118:e2103730118. https://doi.org/10.1073/pnas.2103730118

Nguyen, A., J.M. Loo, R. Mital, E.M. Weinberg, F.Y. Man, Z. Zeng, P.B. Paty, L. Saltz, Y.Y. Janjigian, E. de Stanchina, and S.F. Tavazoie. 2016. PKLR promotes colorectal cancer liver colonization through induction of glutathione synthesis. *J. Clin. Invest.* 126:681–694. https://doi.org/10.1172/JCI83587

Ostendorf, B.N., J. Bilanovic, N. Adaku, K.N. Tafreshian, B. Tavora, R.D. Vaughan, and S.F. Tavazoie. 2020. Common germline variants of the human APOE gene modulate melanoma progression and survival. *Nat. Med.* 26:1048–1053. https://doi.org/10.1038/s41591-020-0879-3

Ostendorf, B.N., M.A. Patel, J. Bilanovic, H.-H. Hoffmann, S.E. Carrasco, C.M. Rice, and S.F. Tavazoie. 2022. Common human genetic variants of APOE impact murine COVID-19 mortality. *Nature*. 611:346–351. https://doi.org/10.1038/s41586-022-05344-2

Pencheva, N., H. Tran, C. Buss, D. Huh, M. Drobnjak, K. Busam, and S.F. Tavazoie. 2012. Convergent multi-miRNA targeting of ApoE drives LRP1/LRP8-dependent melanoma metastasis and angiogenesis. *Cell*. 151:1068–1082. https://doi.org/10.1016/j.cell.2012.10.028

Peng, S.L., A.J. Gerth, A.M. Ranger, and L.H. Glimcher. 2001. NFATc1 and NFATc2 together control both T and B cell activation and differentiation. *Immunity*. 14:13–20. https://doi.org/10.1016/S1074-7613(01)00085-1

Roberts, E.W., M.L. Broz, M. Binnewies, M.B. Headley, A.E. Nelson, D.M. Wolf, T. Kaisho, D. Bogunovic, N. Bhardwaj, and M.F. Krummel. 2016. Critical role for CD103(+)/CD141(+) dendritic cells bearing CCR7 for tumor antigen trafficking and priming of T cell immunity in melanoma. *Cancer Cell*. 30:324–336. https://doi.org/10.1016/j.ccell.2016.06.003

Rodrigues, P.F., A. Kouklas, G. Cvijetic, N. Bouladoux, M. Mitrovic, J.V. Desai, D.S. Lima-Junior, M.S. Lionakis, Y. Belkaid, R. Ivanek, and R. Tussiwand. 2023. pDC-like cells are pre-DC2 and require KLF4 to control homeostatic CD4 T cells. *Sci. Immunol.* 8:eadd4132. https://doi.org/10.1126/sciimmunol.add4132

Schreiber, H.A., J. Loschko, R.A. Karssemeijer, A. Escolano, M.M. Meredith, D. Mucida, P. Guermonprez, and M.C. Nussenzweig. 2013. Intestinal monocytes and macrophages are required for T cell polarization in response to Citrobacter rodentium. *J. Exp. Med.* 210:2025–2039. https://doi.org/10.1084/jem.20130903

Sohrabi, Y., G.V.H. Sonntag, L.C. Braun, S.M.M. Lagache, M. Liebmann, L. Klotz, R. Godfrey, F. Kahles, J. Waltenberger, and H.M. Findeisen. 2020. LXR activation induces a proinflammatory trained innate immunity-phenotype in human monocytes. *Front. Immunol.* 11:353. https://doi.org/10.3389/fimmu.2020.00353

Spann, N.J., and C.K. Glass. 2013. Sterols and oxysterols in immune cell function. *Nat. Immunol.* 14:893–900. https://doi.org/10.1038/ni.2681

Surls, J., C. Nazarov-Stoica, M. Kehl, C. Olsen, S. Casares, and T.-D. Brumeanu. 2012. Increased membrane cholesterol in lymphocytes diverts T-cells toward an inflammatory response. *PLoS One*. 7:e38733. https://doi.org/10.1371/journal.pone.0038733

Swamy, M., K. Beck-Garcia, E. Beck-Garcia, F.A. Hartl, A. Morath, O.S. Yousefi, E.P. Dopfer, E. Molnár, A.K. Schulze, R. Blanco, et al. 2016. A cholesterol-based allostery model of T cell receptor phosphorylation. *Immunity*. 44:1091–1101. https://doi.org/10.1016/j.immuni.2016.04.011

Tavazoie, M.F., I. Pollack, R. Tanqueco, B.N. Ostendorf, B.S. Reis, F.C. Gonsalves, I. Kurth, C. Andreu-Agullo, M.L. Derbyshire, J. Posada, et al. 2018. LXR/ApoE activation restricts innate immune suppression in cancer. *Cell*. 172:825–840.e18. https://doi.org/10.1016/j.cell.2017.12.026

Thaker, Y.R., H. Schneider, and C.E. Rudd. 2015. TCR and CD28 activate the transcription factor NF-κB in T-cells via distinct adaptor signaling complexes. *Immunol. Lett.* 163:113–119. https://doi.org/10.1016/j.imlet.2014.10.020

Törőcsik, D., M. Baráth, S. Benko, L. Széles, B. Dezso, S. Póliska, Z. Hegyi, L. Homolya, I. Szatmári, A. Lányi, and L. Nagy. 2010. Activation of liver X receptor sensitizes human dendritic cells to inflammatory stimuli. *J. Immunol.* 184:5456–5465. https://doi.org/10.4049/jimmunol.0902399

Tumeh, P.C., C.L. Harview, J.H. Yearley, I.P. Shintaku, E.J.M. Taylor, L. Robert, B. Chmielowski, M. Spasic, G. Henry, V. Ciobanu, et al. 2014. PD-1 blockade induces responses by inhibiting adaptive immune resistance. *Nature*. 515:568–571. https://doi.org/10.1038/nature13954

Villablanca, E.J., L. Raccosta, D. Zhou, R. Fontana, D. Maggioni, A. Negro, F. Sanvito, M. Ponzoni, B. Valentinis, M. Bregni, et al. 2009. Tumor-mediated liver X receptor-α activation inhibits CC chemokine receptor-7 expression on dendritic cells and dampens antitumor responses. *Nat. Med.* 16:98–105. https://doi.org/10.1038/nm.2074

Vonderheide, R.H. 2018. The immune revolution: A case for priming, not checkpoint. *Cancer Cell*. 33:563–569. https://doi.org/10.1016/j.ccell.2018.03.008

Wang, F., K. Beck-García, C. Zorzin, W.W.A. Schamel, and M.M. Davis. 2016. Inhibition of T cell receptor signaling by cholesterol sulfate, a naturally occurring derivative of membrane cholesterol. *Nat. Immunol.* 17:844–850. https://doi.org/10.1038/ni.3462

Westerterp, M., E.L. Gautier, A. Ganda, M.M. Molusky, W. Wang, P. Fotakis, N. Wang, G.J. Randolph, V.D. D'Agati, L. Yvan-Charvet, and A.R. Tall. 2017. Cholesterol accumulation in dendritic cells links the inflammasome to acquired immunity. *Cell Metab.* 25:1294–1304.e6. https://doi.org/10.1016/j.cmet.2017.04.005

Weulersse, M., A. Asrir, A.C. Pichler, L. Lemaitre, M. Braun, N. Carrié, M.-V. Joubert, M. Le Moine, L. Do Souto, G. Gaud, et al. 2020. Eomes-dependent loss of the co-activating receptor CD226 restrains CD8+ T cell anti-tumor functions and limits the efficacy of cancer immunotherapy. *Immunity*. 53:824–839.e10. https://doi.org/10.1016/j.immuni.2020.09.006

Yan, C., L. Zheng, S. Jiang, H. Yang, J. Guo, L. Jiang, T. Li, H. Zhang, Y. Bai, Y. Lou, et al. 2023. Exhaustion-associated cholesterol deficiency dampens the cytotoxic arm of antitumor immunity. *Cancer Cell*. 41:1276–1293.e11. https://doi.org/10.1016/j.ccell.2023.04.016

Yang, W., Y. Bai, Y. Xiong, J. Zhang, S. Chen, X. Zheng, X. Meng, L. Li, J. Wang, C. Xu, et al. 2016. Potentiating the antitumour response of CD8+ T cells by modulating cholesterol metabolism. *Nature*. 531:651–655. https://doi.org/10.1038/nature17412

Yeh, J.-H., S.S. Sidhu, and A.C. Chan. 2008. Regulation of a late phase of T cell polarity and effector functions by Crtam. *Cell*. 132:846–859. https://doi.org/10.1016/j.cell.2008.01.013

Yoshida, H., C.A. Lareau, R.N. Ramirez, S.A. Rose, B. Maier, A. Wroblewska, F. Desland, A. Chudnovskiy, A. Mortha, C. Dominguez, et al. 2019. The cis-regulatory atlas of the mouse immune system. *Cell*. 176:897–912.e20. https://doi.org/10.1016/j.cell.2018.12.036

Yukawa, M., S. Jagannathan, S. Vallabh, A.V. Kartashov, X. Chen, M.T. Weirauch, and A. Barski. 2019. AP-1 activity induced by co-stimulation is required for chromatin opening during T cell activation. *J. Exp. Med.* 217:e20182009. https://doi.org/10.1084/jem.20182009

Zamanian-Daryoush, M., D. Lindner, T.C. Tallant, Z. Wang, J. Buffa, E. Klipfell, Y. Parker, D. Hatala, P. Parsons-Wingerter, P. Rayman, et al. 2013. The cardioprotective protein apolipoprotein A1 promotes potent anti-tumorigenic effects. *J. Biol. Chem.* 288:21237–21252. https://doi.org/10.1074/jbc.M113.468967

Zhang, Y., T. Vu, D.C. Palmer, R.J. Kishton, L. Gong, J. Huang, T. Nguyen, Z. Chen, C. Smith, F. Livák, et al. 2022. A T cell resilience model associated with response to immunotherapy in multiple tumor types. *Nat. Med.* 28:1421–1431. https://doi.org/10.1038/s41591-022-01799-y

Supplemental material

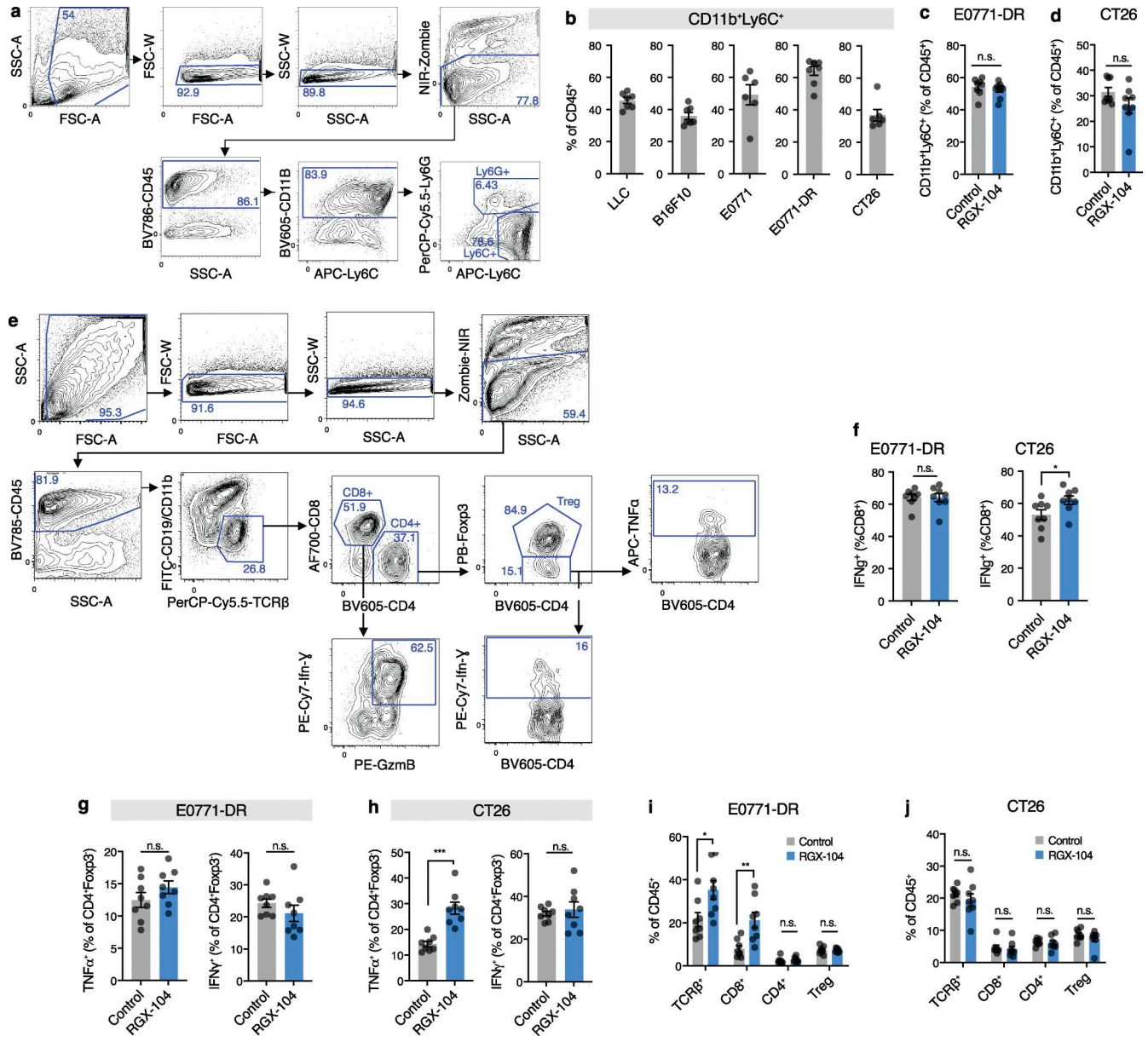

Figure S1. **LXR activation reshapes the tumor immune microenvironment across syngeneic tumor models. (a)** Flow cytometry gating strategy to delineate intratumoral myeloid-derived suppressor cell populations. **(b)** Abundance of CD11b$^+$Ly6C$^+$ M-MDSCs across different cancer models (n = 7, 7, 6, 8, and 6 for LLC, B16F10, E0771, E0771-DR, and CT26, respectively). **(c and d)** Abundance of M-MDSCs in E0771-DR (c) and CT26 (d) tumors upon RGX-104 treatment ($n \geq 8$ per group; two-tailed t test). **(e)** Flow cytometry gating strategy to delineate intratumoral T cell populations. **(f)** Expression of IFN-γ by CD8$^+$ cytotoxic T cells infiltrating E0771-DR and CT26 tumors (n = 8 per group, two-tailed t test, each representative of three and two independent experiments, respectively). **(g and h)** Activation status of intratumoral CD4$^+$Foxp3$^-$ T cells in E0771-DR (g) and CT26 (h) tumors (n = 8 per group, two-tailed t test, each panel representative of two independent experiments). **(i and j)** Proportion of T cell populations of tumor-infiltrating CD45$^+$ cells in E0771-DR (i) and CT26 (j) tumors (n = 8 per group, two-tailed t test, each panel representative of two independent experiments). n.s., nonsignificant; M-MDSC, monocytic myeloid–derived suppressor cells. All panels representative of at least two independent experiments. *P < 0.05, **P < 0.01, and ***P < 0.001.

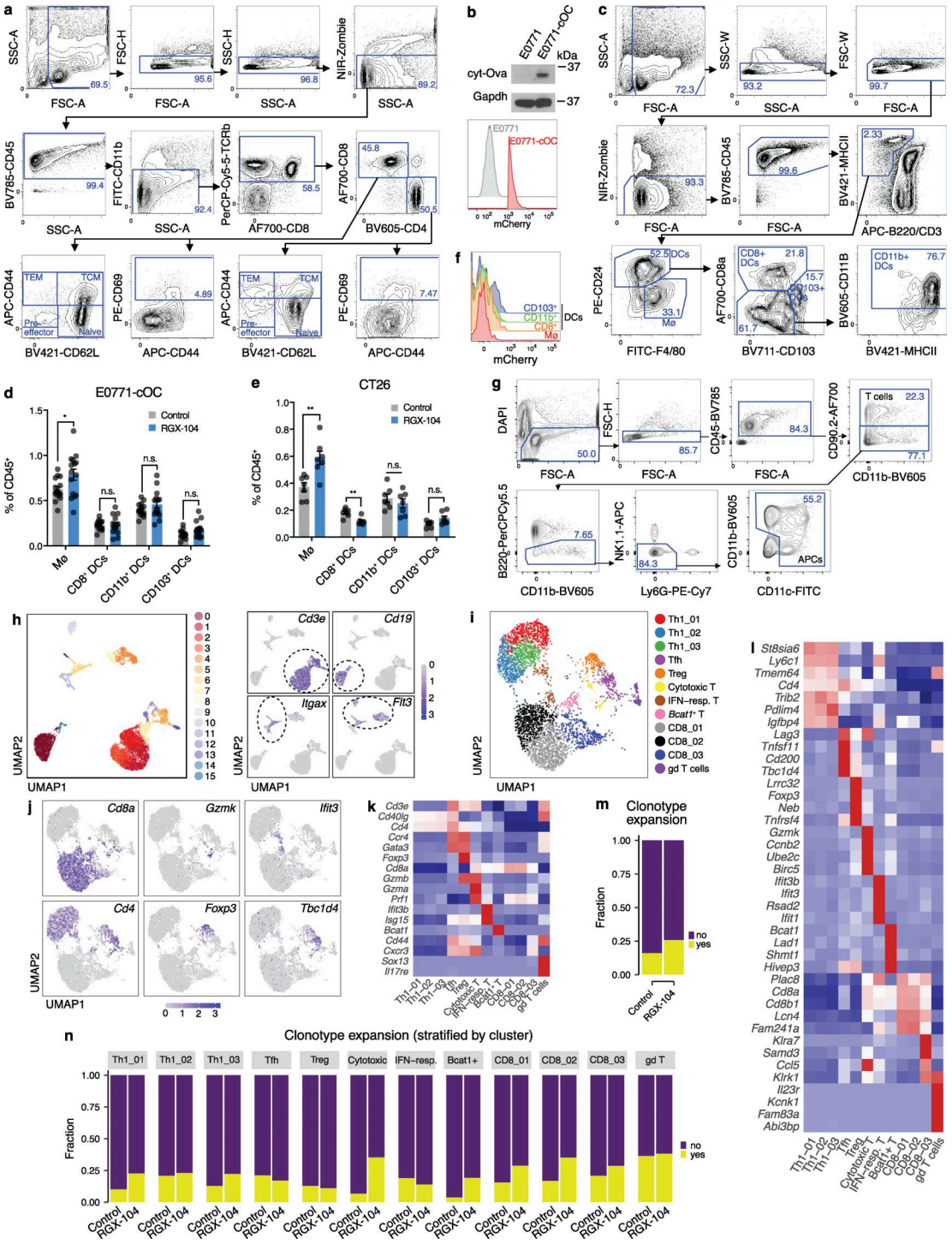

Figure S2. **RGX-104 elicits expansion of rare cytotoxic effector T cells in tumor DLNs. (a)** Gating strategy to delineate T cell activation states in tumor DLNs. **(b)** Expression of cytoplasmic OVA (cyt-OVA) and mCherry in E0771-cOC cells as assessed by western blot and flow cytometry, respectively. **(c)** Flow cytometry gating strategy to delineate APC populations in the DLNs. **(d and e)** Proportion of different APC subsets as percentage of CD45$^+$ leukocytes in LNs draining E0771-cOC (d) or CT26 (e) tumors (n = 15 per group in d, 7 per group in e, two-tailed t test; each representative of two independent experiments). **(f)** Representative example of mCherry fluorescence indicative of uptake of tumor-derived antigen in DLN-resident APC populations. **(g)** Flow cytometric gating strategy to delineate CD45$^+$B220$^-$CD90$^+$ T cells and CD45$^+$CD90$^-$B220-NK1.1$^-$Ly6G$^-$ and CD11b$^+$ or CD11c$^+$ APCs in E0771-DR tumor DLNs. **(h)** UMAP clustering of cells sorted as in g. Plots on the top right show the expression of marker genes indicating T cells (*Cd3e*), contaminating B cells (*Cd19*) and APCs (*Itgax*, *Flt3*). **(i)** UMAP re-clustering of T cells from h. **(j)** Expression of marker genes indicating CD8$^+$ (*Cd8a*), CD4$^+$ (*Cd4*), cytotoxic T cell (*Gzmk*), regulatory T cell (*Foxp3*), IFN-responsive T cell (*Ifit3*), and Tfh (*Tbc1d4*) cell subsets. **(k and l)** Heatmaps indicating average expression of manually curated (k) or top differentially expressed (l) genes per cluster. **(m and n)** Fraction of expanded versus non-expanded clonotypes across all T cells (m) or T cells stratified by subset (n) as assessed by TCRseq in control versus RGX-104–treated mice. MHCII, MHC class II. P < 0.05 and **P < 0.01. Source data are available for this figure: SourceData FS2.

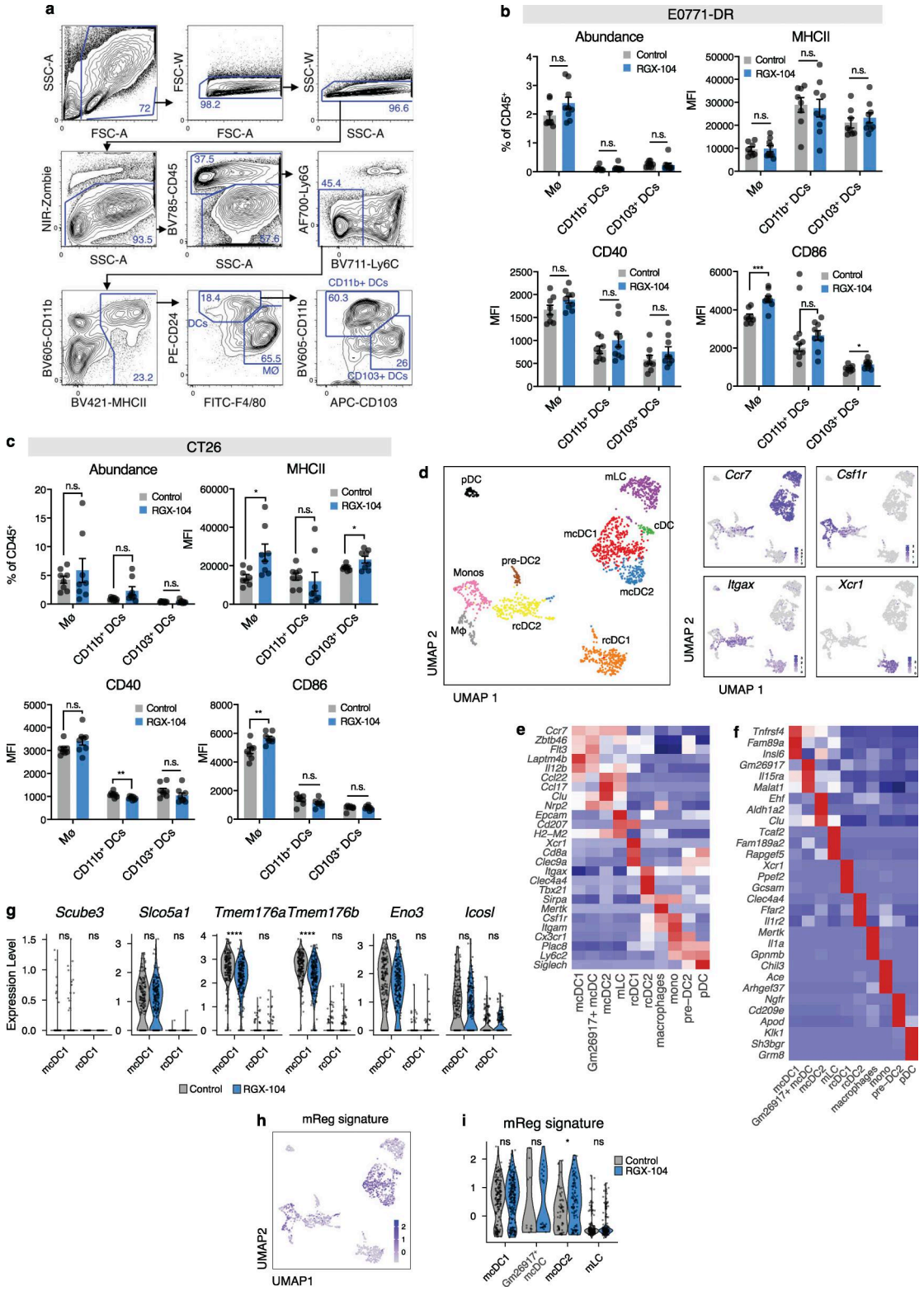

Figure S3. **Phenotyping of tumor- and tumor DLN-resident APCs under LXR-activating therapy. (a)** Flow cytometry gating strategy to delineate major tumor-resident APC subsets. **(b and c)** APC subset abundance and activation status in E0771-DR (b) and CT26 (c) tumors (n = 9 [b] and 8 [c] per group, two-tailed t test; each representative of two independent experiments). **(d)** UMAP clustering of *Itgax* and *Flt3*-expressing APCs from E0771-DR tumor DLNs. Plots on the right show expression of marker genes indicating migratory (*Ccr7*), resident (*Itgax*), myeloid (*Csf1r*), and resident cDC1 (*Xcr1*) APC subsets. **(e and f)** Heatmaps indicating average expression of manually curated (e) or top differentially expressed (f) genes per cluster. **(g)** Expression of genes making up the tolerogenic maturation gene expression signature (Bosteels et al., 2023) in cDC1 subsets from d. **(h)** Expression of the mReg regulatory signature (Maier et al., 2020) in tdLN APCs as assessed by scRNAseq from d. **(i)** Comparison of the expression of the mReg regulatory signature in migratory DC subsets in control versus LXR agonist–treated mice from d. MHCII, MHC class II. *P < 0.05, **P < 0.01, ***P < 0.001, and ****P < 0.0001.

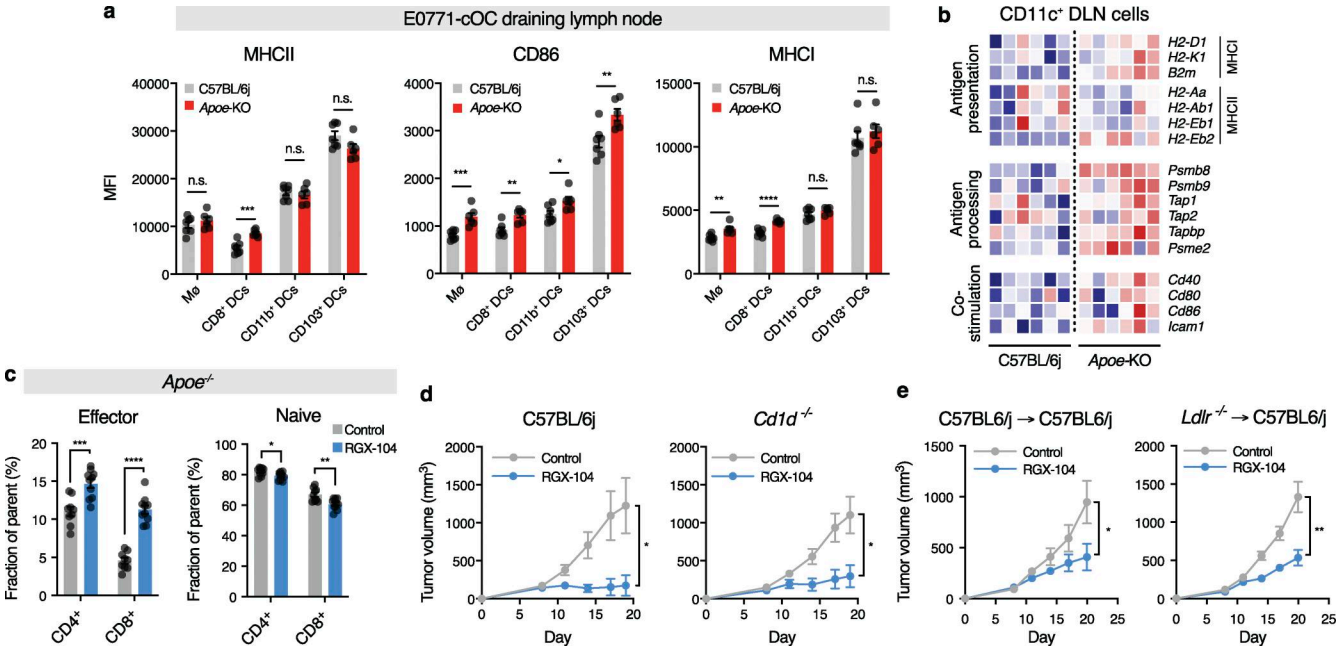

Figure S4. **LXR agonism in breast cancer models exerts therapeutic anti-tumor activity independent of the Apoe/Ldlr/Cd1d axis. (a and b)** Expression of activation markers as assessed by flow cytometry (a) and RNAseq (b) in APCs in E0771-cOC tumor DLNs in wild-type versus *Apoe-KO* mice ($n \geq 6$–7 per group, two-tailed *t* test). **(c)** Phenotype of DLN-resident T cells in *Apoe*$^{-/-}$ E0771-cOC tumor-bearing mice treated with RGX-104 ($n \geq 9$ per group, respectively, two-tailed *t* tests). **(d)** Growth of orthotopic E0771-DR tumors in C57BL6/J versus NKT-cell deficient *CD1d*-KO mice ($n \geq 6$ per group, data representative of two independent experiments). **(e)** Growth of E0771-DR tumors in mice transplanted with wild-type or *Ldlr*-KO bone marrow ($n \geq 7$ per group). MHCII, MHC class II. *P < 0.05, **P < 0.01, and ***P < 0.001.

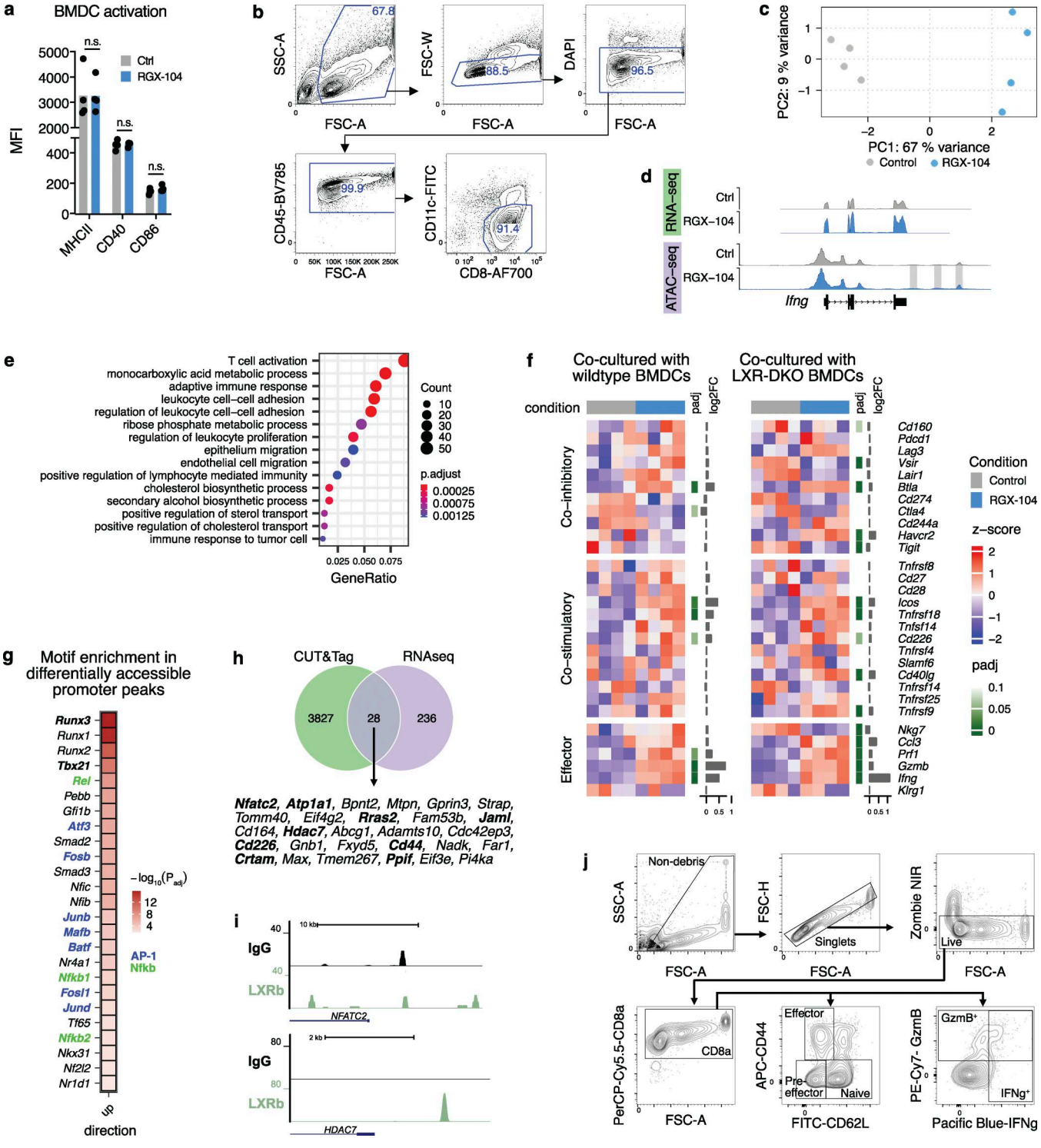

Figure S5. **Extended analysis of the impact of RGX-104 on DC/T cell interplay. (a)** Impact of LXR agonistic treatment on expression of activation markers in BMDCs (n = 4 per group, representative of four independent experiments; P values according to two-tailed T tests). **(b)** Gating strategy for flow cytometric sorting of CD8⁺ OT-I T cells upon co-culture with BMDCs. **(c)** Principal component analysis of OT-I T cell samples subjected to RNAseq. **(d)** RNAseq and ATAC-seq tracks for the *Ifng* gene in OT-I CD8⁺ T cells co-cultured with LXR^{DKO} BMDCs upon RGX-104 treatment as assessed by RNAseq and ATAC-seq. **(e)** Gene ontology pathway enrichment analysis of genes significantly upregulated in RGX-104–treated OT-I T cells co-cultured with LXR^{DKO} BMDCs. **(f)** RNAseq of OT-I CD8⁺ T cells co-cultured with wild-type (left) or LXR-deficient (right) BMDCs. **(g)** Enrichment of transcription factor–binding sites in differentially accessible chromatin promoter regions of RGX-104–treated OT-I T cells co-cultured with LXR^{DKO} BMDCs (adjusted P values according to Fisher exact tests). **(h)** Overlap of genes showing upregulation in CD8⁺ T cells upon pharmacological LXR activation and with binding of LXRb to their promoter regions as assessed by CUT&Tag. Genes displayed in bold are genes with known roles in shaping T cell activation/function. **(i)** Gene tracks depicting CUT&TAG signal near promoter regions of indicated T cell effector–relevant target genes for IgG control CUT&TAG (black) or LXRb CUT&TAG (green) samples. **(j)** Flow cytometry gating hierarchy for assessing in vitro treatment of primary naive CD8⁺ T cells.